

Contents lists available at ScienceDirect

Journal of the Mechanics and Physics of Solids

journal homepage: www.elsevier.com/locate/jmps



A microstructure-based approach to modeling electrostriction that accounts for variability in spatial locations of domains



Anil Erol*, Saad Ahmed, Zoubeida Ounaies, Paris von Lockette

Department of Mechanical and Nuclear Engineering, The Pennsylvania State University, University Park, PA 16802, USA

ARTICLE INFO

Article history:
Received 22 February 2018
Revised 1 September 2018
Accepted 22 September 2018
Available online 22 September 2018

ABSTRACT

The discovery of polyvinylidene fluoride (PVDF) based family of relaxor ferroelectric (RFE) polymers has attracted attention due to their high electrostrictive strain and relatively low hysteresis loss. These RFE polymers exhibit complex microstructures containing both crystalline domains and amorphous domains; the interactions of the crystalline domains drive the electrostrictive behavior of these EAPs, while the amorphous domains dictate the mechanical behavior of the materials. Furthermore, the crystalline domains are spatially and orientationally distributed across the amorphous medium, further complicating the morphology of RFE polymers. Although a number of studies have focused on experimental and computational investigation of the interaction among different crystalline phases of this family of RFE, electrostriction models that represent the variabilities in the microstructure of biphasic RFE polymers are lacking. The proposed model aims to link the semicrystalline microstructure to the observed electromechanical coupling. An energy density function is constructed for a representative volume element (RVE) of the EAP, including a term for each phase, crystalline and amorphous. The interaction of the crystalline domains is based on the Coulomb interaction energy between a pair of dipoles. The responses of the amorphous domains are predicted by a modified hyperelastic stress-stretch eight-chain model. The total free energy is then analyzed under constitutive laws for an isothermal electromechanical deformation to determine the stresses generated in the RVE. The strain versus electric field, i.e. the electrostriction, relationship is calculated from a self-equilibrium condition of the Cauchy stress. The microstructure of the material is taken into account by applying the dipolar energy to a semicrystalline network model, in which a dipole that represents a crystalline domain is surrounded by an amorphous medium. The semicrystalline RVE experiences interactions with neighboring crystallites, which drives the electrostriction of the material. Two basic cases of the semicrystalline network model are explored to study the effects of spatial variation of crystalline domain locations relative to each other. Furthermore, higher fidelity descriptions of spatial location are introduced through the addition of a probability density function (PDF) of dipoles around a central dipole. Comparing the model to experimental results from the literature allows best-fit determination of the model parameters describing the PDF, e.g. aspects of microstructure, itself. These results,

E-mail address: axe944@psu.edu (A. Erol).

^{*} Corresponding author.

which agree well with experimental data, imply that the model has an ability to infer key information about the microstructure of the material by fitting the distribution of dipoles with a single adjustable parameter. The model is unique in that its descriptions of the crystalline domains is amenable to direct measurement by spectroscopic scattering techniques. Consequently, adjustable parameters in the model are linked to physical characteristics that are quantifiable, such as magnitudes of dipole moments and spatial distribution parameters. The model may also be used to elucidate aspects of network morphology using best fit of these physically meaningful adjustable parameters to experimental data, possibly providing a link between processing-structure-property relationships for future researchers.

© 2018 Published by Elsevier Ltd.

1. Introduction

1.1. Microstructure-property relationship in PVDF-based RFE polymers

Electro-active polymers (EAPs) have gained significant attention over the years for their high electromechanical responses (Bar-Cohen, 2002; Zhang et. al., 1998). Among EAPs, polyvinylidine fluoride, P(VDF), and its copolymer polyvinylidine-fluoride trifluoroethyline, P(VDF-TrFE), are ferroelectric materials that derive their electromechanical properties from ferroelectric domains (Dang et. al., 2003; Nalwa, 1995). More recently, a bulky third monomer was added to the copolymer to deliberately generate defects in the microstructure, breaking down crystalline phase into nano-polar domains (Xu et al., 2001; Ang et al. 2005). As a result, new PVDF-based terpolymers with relaxor ferroelectric (RFE) properties were developed. Two types of PVDF-based terpolymers are poly (vinylidene-fluoride-trifluoroethylene-chlorofluoroethylene), and poly (vinylidene-fluoride-trifluoroethylene-chlorotrifluoroethylene), also known as P(VDF-TrFE-CFE) and P(VDF-TrFE-CTFE), respectively (Bauer et al., 2002; Chu et al., 2006; Xu et al., 2001). The terpolymers mainly differ from ferroelectric materials by exhibiting a slim hysteresis loop in their polarization response, as shown in dashed line in Fig. 1, (Klein et al., 2005; Xu et al., 2001), which was ascribed to the semicrystalline structure of PVDF-based RFE polymers containing mobile crystalline phases within an amorphous phase (Lu et al., 2008; Xu et al., 2001).

Electrostriction in the PVDF-based polymers is dependent on the presence of both crystalline and amorphous phases. Greater presence of the amorphous phase yields greater strains by reducing the stiffness of the material (Lu et al., 2006), while more crystalline phase content increases the polarization response. Thus, researchers studied the tradeoff between the two phases by varying the chemical composition of PVDF-based terpolymers, aiming to tailor the electromechanical properties in a precise fashion (Klein et al., 2005; Lu et al., 2006; Yang et al., 2013). Specifically, increasing the percentage of CTFE expanded the amorphous phase, and reduced the crystal domain sizes (Xu et al., 2001) and their separation distances (Yang et al., 2013), which provided more room between crystalline domains, allowing domains to rotate with less friction. Moreover, an increase in crystallinity increased the stiffness of the material (Lu et al., 2006). These findings indicate that by varying just the chemical composition, researchers can affect the microstructure to modify the electrostrictive response of these PVDF-based RFE polymers.

Several studies have shown that processing steps significantly affect the microstructure and thereby bulk material properties of RFE polymers. Studies performed by Sencadas et. al. (2009), Silva et al. (2010), explored how the crystallinity and microstructural variations of PVDF, the primary monomer of the RFE polymers, were affected by temperature, processing methods, and other variables. Bao et al. (2007) observed that for the same composition of PVDF-based terpolymer, different processing conditions affected the amount of polar nanodomains in the material. Smith et al. (2014), discovered through SEM images that thermal treatments with a slow quenching process allowed for larger crystal domain formation during the crystallization process, with fibrillary shape characteristics, and these changes in the microstructure increased the dielectric constant of the material. Cho, et al. (2016) confirmed these results by comparing fabrication methods with and without thermal treatments above the transition temperature of the terpolymer, which results in the dominance of different types of crystalline phases, such as the α -, β - and γ - phases. The results of Cho, et al. (2016) also showed that thermal treatments produce largely α -phase dominant microstructures, while room temperature crystallization produces the larger β -phase crystallites; the crystallization process is important because the shifting of phases affects the electrostrictive response of the material. Ultimately, these findings imply that the shapes, sizes, and phase type of crystalline domains are all important factors in the overall electromechanical response mechanism of PVDF-based EAPs and, furthermore, may be controlled, providing an avenue to tailored electromechanical response.

1.2. Modeling of hyperelasticity and relaxor ferroelectric EAPs

The first part of this section will consider previous modeling methods for the hyperelastic response of polymers, and the latter part will survey tools and methods for combining hyperelasticity theory with electrodynamics. Later, approaches to incorporate orientation and spatial distribution information will be discussed, leading to the focus of this work, which is to address the orientational polarization of the crystalline domains within a coupled hyperelastic framework.

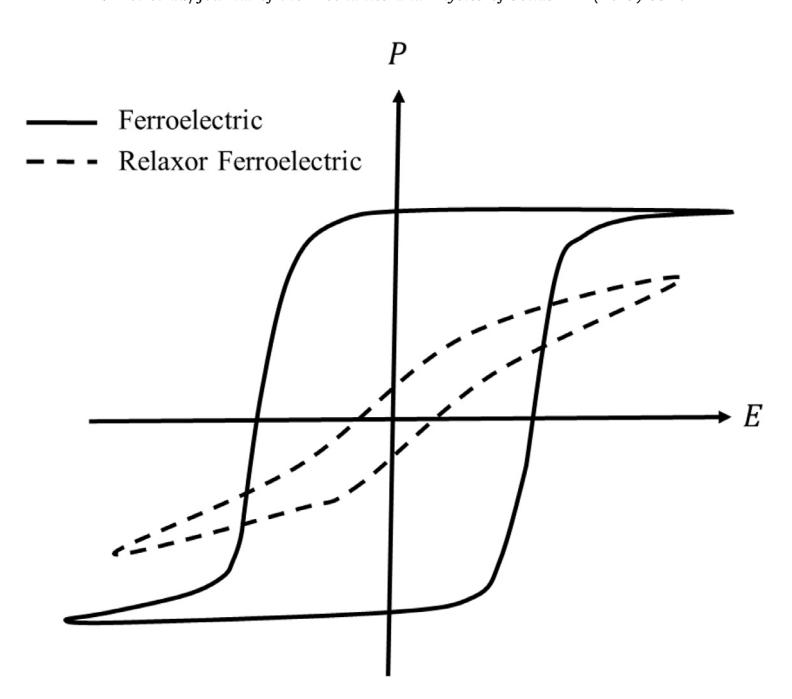


Fig. 1. Polarization curves for a ferroelectric material and a relaxor ferroelectric material.

Polymers can exhibit high strains that reach beyond the limits of classical Hookean mechanics, such that a linear model employing Young's modulus as a constant is not sufficient in predicting the elastic response of the material (Mooney, 1940). However, the only extant model that incorporates both non-polar amorphous and polar crystalline phases is based in linear elasticity (Capsal et al., 2012). In many works and herein, the mechanical deformation of polymers is assumed to be governed by a nonlinear model that captures experimentally observed response.

Invariant-based modeling was a method adopted initially to characterize hyperelastic materials. Rivlin (1948) developed a generalized infinite series to predict the behavior of elastic materials in the form of

$$W = \sum_{i=0}^{\infty} \sum_{j=0}^{\infty} C_{ij} (I_1 - 3)^i (I_2 - 3)^j, \tag{1}$$

in which C_{ij} were constants, and I_1 and I_2 were the principle invariants, defined as functions of the principal invariants of the right Cauchy Green deformation tensor,

$$I_1 = tr(\mathbf{F}^T \mathbf{F}), \tag{2}$$

$$I_2 = \frac{1}{2} \left[\left(tr(\mathbf{F}^T \mathbf{F}) \right)^2 - tr\left(\left(\mathbf{F}^T \mathbf{F} \right)^2 \right) \right]$$
 (3)

The deformation gradient F is defined in Section 2.

The model that Rivlin (1948) proposed was a first order approximation of the infinite series in (1). This first-order approximation is commonly known as the Neo-Hookean model, and with the form of

$$W = C_{10}(I_1 - 3) \tag{4}$$

To provide a better fit to experimental data, the Mooney-Rivlin model added the i=0, j=1 term of (1)–(4) Rivlin, 1948). Following this trend, later models added terms to ((4). More recently, Ogden (1997) developed a constitutive model utilizing an indefinite number of stretch-based terms to obtain a widely adjustable fit to rubber elasticity response. However, the primary disadvantage to invariant-based and stretch-based modeling was that the coefficients scaling each term in the series did not represent physical quantities; attribution to physical quantities only came with additional assumptions of structure not presented in the original models. We seek a model in which adjustable parameters are tied directly to physical quantities, allowing the model to aid understanding of the relationship between microstructure and electrostrictive response.

In contrast to invariant- and stretch-based hyperelastic modeling, Treloar (1944) began building the framework for phenomenological constitutive modeling by exploring the statistical mechanics of polymer chains for rubber. Treloar (1943) constructed a strain energy function for the elastic response of rubber, the form of which is shown in (5).

$$W = \frac{1}{2}NkT(I_1 - 3) \tag{5}$$

In (5), N is the chain-density, k is Boltzmann's constant, T is absolute temperature, and λ_i are the principal stretches for i=1,2,3 in a principal coordinate space. This model's significance was its ability to capture the behavior of rubbers based on polymer chain mechanics. Furthermore, its form was similar to the Neo-Hookean model and thus offered a physical meaning to the coefficient C_{10} such that $C_{10} = \frac{1}{2}NkT$ was proportional to the initial 'rubbery' modulus. Though the model was based on a statistical description of a physical chain (i.e. Gaussian chains), the model did not account for the locking stretch, and consequently did not provide a link to material structure. While the formulation in (5) is for a single polymer chain, the same theoretical methodology has been applied to more complex representations of polymer networks such as the three-chain network (Wang and Guth, 1952) and the four chains (i.e. tetrahedral) network models (Flory and Rehner, 1943). In addition to these models, an eight-chain model was developed by Arruda and Boyce (1993), apportioning the energy of the network, still computed through random walk by statistics, to a deforming unit cube geometry under affine deformation in the principal space. Arruda and Boyce (1993) discovered that the additional chains provided a better fit to experimental data across multiple deformation states, arguably because the diagonal orientations of the chains provide wider spatial averaging of polymer network behavior. While the efficacy of wider averaging of the network has been shown for purely elastic behavior, it will be explored in this work with regards to electromechanical coupling, specifically concurrent averaging across spatial and orientation distributions of electric dipoles of the crystalline regions of a PVDF-based RFE polymer.

The electromechanical deformation of dielectric materials has been extensively studied since the 1950s, Toupin (1956) first developed the field equations for deformable dielectric materials, where the energy density of the material, U_r , was determined to be a function of the relative electric permittivity, ϵ_r , and quadratically related to the electric field E, such that $U = (1/2)\epsilon_r \epsilon_0 E^2$; others improved on the field equations in the following years (Eringen, 1963; Truesdell and Toupin, 1960). Recent additions have been made to the list of dielectric and other active material models that have each added new concepts or mechanisms, such as deformation dependent permittivities (Zhao and Suo, 2009; and Jimenez and McMeeking, 2013); a free energy consisting of multiple components attributed to electrostrictive, elastic, dielectric, and residual dielectric energies (Richards et al., 2010); viscoelasticity (Ask et. al., 2015; Hong, 2011); hysteresis of ferroelectrics (Lallart et al., 2016); multiplicative electro-elasticity (Skatulla et. al., 2012; Zah and Miehe, 2015); electroplasticity (Miehe, 1998); variational frameworks that model microstructural evolutions of domains in ferroelectric ceramics (Miehe et. al., 2012); multi-scale methods that account for micro-scale dipole rotations (Cohen, 2014); and homogenization methods that study the effects of particle sizes and distributions on active material properties (Castaneda et al., 2012; Zah and Miehe, 2013). These models have sought to improve existing electro-elastic theories by adding methods that address various complexities of EAP modeling, but they have not developed semicrystalline microstructure-based modeling of electrostriction that address micro-scale spatial orientation, and none have specifically modeled the response of RFE polymers.

Recent work has suggested that microscale spatial organization of polycrystalline polarizable regions within a PVDF-based RFE polymer affects its macroscale electromechanical coupling. Guan et al. (2010) discussed the importance of interactions between ferroelectric domains within an amorphous matrix for PVDF-based polymers, and developed a rudimentary model to predict the depolarization fields for this type of microstructure. The authors pointed out that there was anisotropy in the interactions of polar domains, based on dipole-dipole interactions, and concluded that the relative locations of domains were an important factor in the polarization of semicrystalline EAPs. However, Guan et al. (2010) did not analyze the electromechanical coupling of their semicrystalline model. The framework proposed herein will account for the anisotropic behavior of dipole-dipole interactions and their spatial organization when computing electrostriction.

Only recently did models emerge in the field of EAPs that have incorporated physical elements of the microstructure of the material to the deformations observed in experiments, although note these works focused on dielectric elastomers, not RFE polymers (Cohen, 2014; Cohen and deBotton, 2015). Cohen and Dayal 2016 introduced a method in which the polymer network is defined as a segment of a circular chain composed of rigid rods (unit elements) that represent dipoles—which is an interpretation of the microstructure of dielectric elastomers. The alignment of those dipoles under an electric field subsequently generates a deformation in the chain. This model shows promise due to its ability to consider various modes of deformation of individual unit elements within a network model that ties the mechanics of polymer chains to the electrostriction of the material, thus enabling the model to address information within the microstructure in an electrostriction modeling framework. However, since the model represents dielectric polymers with a single phase, it is not applicable to semicrystalline RFE polymers.

Zah and Miehe (2015) proposed a model (for graft elastomers) with a semicrystalline physical basis. Their model assumed that graft elastomers generated electromechanical strain through the rotations of crystals that pull together neighboring chains via crosslinks. This mechanism, however, is less relevant for PVDF-based RFE polymers, which do not have crosslinks in their microstructure. Instead, dipole-dipole interactions will drive the electromechanical mechanism for RFE polymers, as discussed by Guan et al. (2010).

Capsal et al. (2012) developed a model that accounted for the *biphasic* constitution of RFE polymers by splitting the bulk polarization response of the material into separate contributions from the amorphous and crystalline phases. In addition, their model incorporated an averaging method for the orientational distribution of dipoles. However, the model did not address the spatial locations of the crystalline domains, a primary characteristic in determining their interaction. Further, the model calculated electromechanical strain using a linear elasticity. While we similarly propose the use of a biphasic model, our microstructural representation of dipole arrangements will account for spatial location and orientation; we further assume a hyperelastic material response.

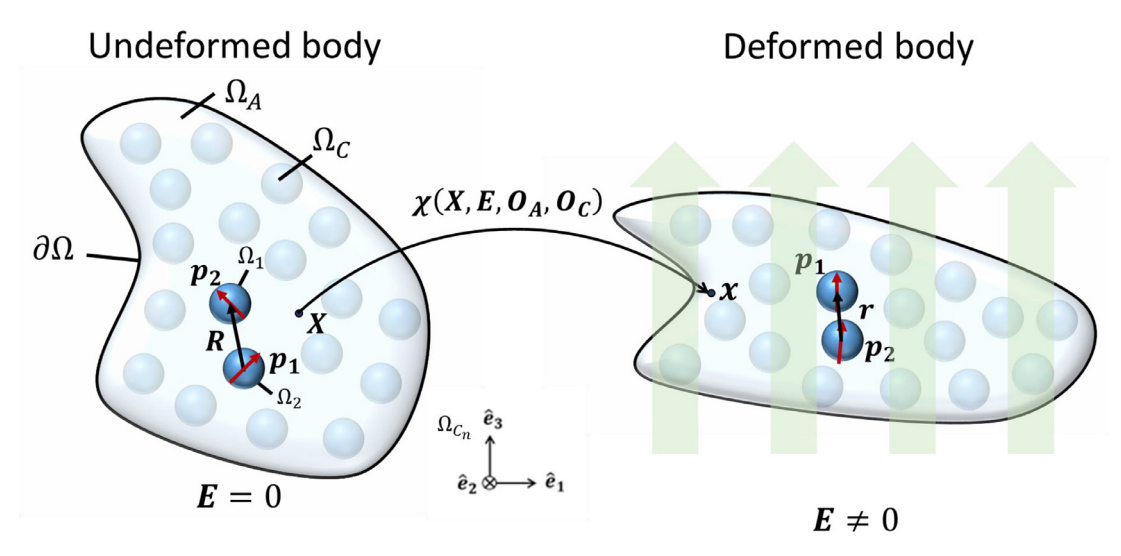


Fig. 2. Two-dimensional schematic of a biphasic body (i.e., a body with inclusions) undergoing deformation. The left body is in the undeformed configuration and the body on the right is in the deformed configuration.

In summary, PVDF-based polymers are semicrystalline polymers, requiring models that describe their biphasic, crystalline and amorphous, constitution. The spatial and orientation distributions of these polarizable crystalline regions, which may be controlled through composition and processing, affect electromechanical coupling and hence are important quantities to any modeling attempt. The spatial organization of the crystalline regions formed in these relaxor ferroelectric (RFE) polymers during processing varies, requiring the development of a model capable of capturing what is known about terpolymer morphology. Thus, the main goal of this study is to construct an appropriate network model for a P(VDF)-based relaxor RFE polymer that ties microstructure to electromechanical coupling by incorporating chain mechanics for polymeric response; spatial and orientation averaging methods of polarizable domains' relative locations and orientations; and a representation of the material's semicrystallinity, i.e. its biphasic constitution. A secondary purpose of this model is to guide future researchers in choosing a target design for the microstructure of a dipole-based material in terms of domain arrangements in order to achieve their desired material properties. Thus, the model will build a foundation for more complex analyses on understanding the relationship between specific parameters within the microstructure and bulk properties of the material.

2. Modeling framework

In this section, mechanics of the problem are briefly summarized. These equations will be later implemented to solve for electromechanical relations for the framework provided in Section 3.

2.1. Kinematics of a semicrystalline, electrostrictive body

The discussion begins by defining a body Ω consisting of two phases (see Fig. 2). It is assumed that there are distinct boundaries at the interfaces between the two phases, such that the two phases are contained in separate domains. An amorphous phase is contained in the nominally contiguous subspace, Ω_0 , and the crystalline phases are a collection of discrete domains within the subspaces, Ω_i (for $i = 1, 2, ..., N_c$). The subspaces are defined such that

$$\Omega = \Omega_0 \cup \Omega_{C_1} \cup \Omega_{C_2} \cup \ldots \cup \Omega_{N_c} \tag{6}$$

Fig. 2 illustrates the deformation of Ω , which can be represented by the linear mapping χ between the undeformed body, and the deformed body. The position vectors in the undeformed and the deformed configurations are \mathbf{X} and \mathbf{x} , respectively. The deformation χ can be written as a function of the position vectors in the reference configuration, \mathbf{X} , as well as other parameters that affect the deformation, such that $\chi = \chi(X, E, \mathbf{0})$, where \mathbf{E} is the applied electric field and $\mathbf{0} = \{\mathbf{0}_A, \mathbf{0}_C\}$ contains sets of parameters relating to the properties of the amorphous and crystalline phases of the material. For simplicity, the bases in both configurations are prescribed as the orthonormal set, $\{\hat{e}_1, \hat{e}_2, \hat{e}_3\}$. The components of the deformation gradient of Ω are defined in the reference configuration by

$$\mathbf{F} = \frac{\partial \chi(\mathbf{X}, \mathbf{0})}{\partial \mathbf{X}} = \nabla_{\mathbf{X}} \mathbf{X} \tag{7}$$

In (7), **F** is the deformation gradient, which is a second-order tensor, and ∇ is the gradient operator in a three-dimensional point space. The left and right Cauchy–Green deformation tensors are defined in terms of the deformation

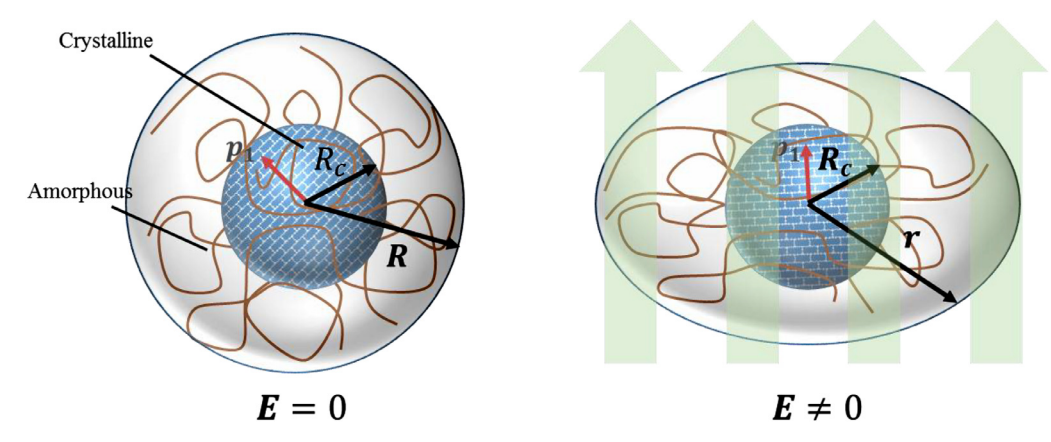


Fig. 3. The representative volume element contains a spherical crystalline domain, surrounded by a concentric amorphous domain that is initially spherical and deforms into an ellipsoidal shape after deformation.

gradient by the relations, respectively,

$$B = FF^{T}, (8)$$

$$C = F^T F \tag{9}$$

Expressing any vector \mathbf{R} between any two crystalline domains Ω_i and Ω_j in the undeformed configuration in terms of the basis vectors yields

$$\mathbf{R} = R_1 \hat{\mathbf{e}}_1 + R_2 \hat{\mathbf{e}}_2 + R_3 \hat{\mathbf{e}}_3. \tag{10}$$

where R_k represents the component of **R** in $\hat{\boldsymbol{e}}_k$ for k=1,2,3. After deformation $\boldsymbol{\chi}$,

$$r = FR. (11)$$

The magnitude of r can be expressed as

$$r^2 = FR \cdot FR \tag{12}$$

We assume Ω undergoes affine deformation, and further that crystalline domains Ω_i are free to rotate. The relatively large stiffness of the crystalline phase with respect to the amorphous phase strongly apportions stretch to the amorphous phase. Consequently, crystalline regions are assumed to be rigid. Additionally, the rotations of the crystalline regions will have no impact on the elastic or dielectric response of the material. These assumptions follow findings of Yang et al (2013). For the purpose of this study, we choose a representative volume element (RVE) composed of a single spherical crystalline region surrounded by a spherical amorphous region, as shown in Fig. 3.

Given the assumptions made on the crystalline regions (rigidity and ability to freely rotate), any polarization vector $\mathbf{p_i}$ of any domain Ω_i is a function of \mathbf{E} and \mathbf{O} . This implies that $\mathbf{p_i}$ may be assumed to be uninfluenced by mechanical deformation. The field-dependent form of $\mathbf{p_i}$ will be later defined by electrodynamics.

Based on the symmetry of the RVE, a differential element can be drawn similar to the proto-type semicrystalline chain developed by Nateghi et al. (2018). In this prior work, the crystalline region is represented as a straight, rigid line segment while the amorphous region continues from the end of the crystalline segment along a representative random walk. Considering this type of element will allow us to write the kinematics of the semicrystalline RVE in terms of the micro-stretch, and relate it to the macro-stretch. The newly defined semicrystalline element in Fig. 4 occupies an infinitesimal region in space, which is divided among the two phases. In our work, the crystalline region is indicated by ordered, rectilinear chain paths, while the amorphous region contains less ordered paths resembling a random walk. In Fig. 4, the left element is in the undeformed configuration, and the right element is in the deformed configuration; the configurations are annotated with their respective notations, and each adopt an appropriate spherical coordinate system, as depicted in Fig. 4.

The element contains a rigid crystalline region of length $r_c \equiv R_c$, and a deforming amorphous region of length r_A (see Fig. 4). The total length of the semicrystalline element in the undeformed state is $R_{SC} = R_C + R_A$, and in the deformed state, $r_{SC} = r_C + r_A$, which can be related to the macroscopic deformation by the relations in (11) and (12). A spherical coordinate system is adopted for the undeformed and deformed configurations, as depicted in Fig. 4. The subscript "sc" denotes parameters used for the semicrystalline differential element.

Following Nateghi et al. (2018), although the crystalline region is assumed rigid (relatively), the amorphous region may stretch, yielding the relationship $r_A = \lambda_A R_A$, where λ_A is the stretch of the amorphous region. The stretch along \mathbf{r} of the two-segment element, λ , can be defined as,

$$\lambda = \frac{\lambda_A R_A + R_C}{R_A + R_C} \tag{13}$$

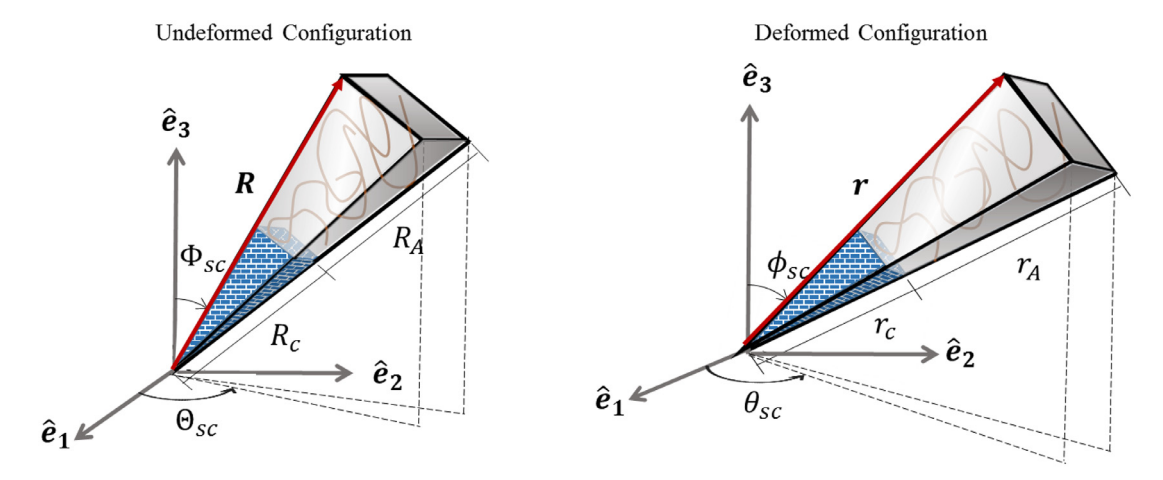


Fig. 4. The deformation of a segmented element consisting of crystalline and amorphous phases is presented.

The length of the crystalline segment can be determined if the material's percent crystallinity X_c is known, and defined as

$$V_c = \nu_c V \tag{14}$$

where V_c is the volume occupied by the crystalline phase, and V is the total volume of the RVE. These volumes are spherical, which yields

$$V = \frac{4\pi}{3}R^3 \tag{15}$$

$$V_c = \frac{4\pi}{3} R_c^{\ 3} \tag{16}$$

Eqs. (14)-(16) can be combined to determine the initial lengths of the crystalline and amorphous regions,

$$R_c = \nu_c^{\frac{1}{3}} R$$

$$R_A = \left(1 - \nu_c^{\frac{1}{3}}\right) R \tag{17}$$

which can be substituted into (13) to yield

$$\lambda = \lambda_A \left(1 - \nu_c^{\frac{1}{3}} \right) + \nu_c^{\frac{1}{3}} \tag{18}$$

Eq. (18) relates the semicrystalline element's stretch to the crystallinity of the material and the stretch of the amorphous segment. If the material contains 0% crystalline phase, then $v_c = 0$, yielding $\lambda = \lambda_A$. Conversely, if the material is 100% crystalline, then $v_c = 1$, and $\lambda = 1$ (completely rigid). This equation is thus a good start for the relation between the total chain stretch and the amorphous segment stretch, but must still be related to macroscopic deformation.

The semicrystalline element's stretch can be related to the macroscopic stretches by writing r_{sc} in terms of its components r_1 , r_2 , and r_3 ,

$$r^2 = r_1^2 + r_2^2 + r_3^2, (19)$$

where $r_i = \mathbf{r} \cdot \hat{\mathbf{e}}_i$ for i = 1,2,3. Relating each component to the undeformed total length and macroscopic stretches,

$$(\lambda R)^{2} = (\lambda_{1}R_{1})^{2} + (\lambda_{2}R_{2})^{2} + (\lambda_{3}R_{3})^{2}$$
(20)

By following a procedure similar to Wu and van der Giessen (1993), we relate the components of the semicrystalline element's length to the element's orientation in the undeformed configuration,

$$R_1 = R\sin\Phi\cos\Theta,$$

 $R_2 = R\sin\Phi\sin\Theta,$
 $R_3 = R\cos\Phi,$
(21)

which yields

$$\lambda = \sqrt{\left(\sin\Phi\cos\Theta\lambda_1\right)^2 + \left(\sin\Phi\sin\Theta\lambda_2\right)^2 + \left(\cos\Phi\lambda_3\right)^2} \tag{22}$$

The relation in (22) can be combined with (18) to write λ_A in terms of the principal stretches,

$$\lambda_{A} = \frac{1}{(1 - \nu_{c})} \sqrt{\left(\sin\Phi\cos\Theta\lambda_{1}\right)^{2} + \left(\sin\Phi\sin\Theta\lambda_{2}\right)^{2} + \left(\cos\Phi\lambda_{3}\right)^{2}} - \frac{\nu_{c}}{(1 - \nu_{c})}$$
(23)

Similarly, λ_A may be written in an Eulerian description as $\lambda_A()$,

$$\lambda_{A} = \frac{1}{(1 - \nu_{c})} \left[(\sin\phi \cos\theta)^{2} \lambda_{2}^{-2} + (\sin\phi \sin\theta)^{2} \lambda_{2}^{-2} + (\cos\phi)^{2} \lambda_{3}^{-2} \right]^{-1/2} - \frac{\nu_{c}}{(1 - \nu_{c})}$$
(24)

The derivation of $\lambda(\phi, \theta)$ can be found in Wu and van der Giessen (1993).

For later calculations, it will also be convenient to express the principal stretches of only the amorphous region, which are denoted by λ^A_i . The relations between the components of r, r, and r, can be established as

$$r_i = r^c_i + r^A_i \tag{25}$$

where $r^c_i = r_c \cdot \hat{e}_i$ and $r^A_i = r_A \cdot \hat{e}_i$ (superscripts not to be confused with contravariant components). Similar to the procedure used to obtain (20), we can write

$$\lambda_i R = R_c + \lambda^A_i R_A \tag{26}$$

and with the help of (17), substitutions for R_c and R_A can be made. After rearranging (25), λ^A_i can be determined,

$$\lambda_i^A = \frac{\lambda_i - \nu_c^{\frac{1}{3}}}{1 - \nu_c^{\frac{1}{3}}} \tag{27}$$

2.2. Traction-free equilibrium

The electrostrictive material is assumed to have an electromechanical strain energy-density, W. The Cauchy stress, T, can be written as a function of W by a constitutive law between W and T derived for an isothermal, electromechanical process (developed by Richards, et al. (2010) via the Clausius-Duhem inequality). Thus, the expression for T is given by

$$T = \frac{2}{I} \frac{\partial W}{\partial \mathbf{B}} \mathbf{B} + q \mathbf{I},\tag{28}$$

where q is a Lagrange multiplier enforcing the incompressibility constraint, and I is the second order identity tensor. In describing the behavior of a small section of this electrostrictive material, it is assumed the body is traction-free and its boundary $\partial\Omega$ is not subjected to any constraints on deformation. These assumptions represent traction free self-equilibrium (free deformation), I = 0.

From (28), the forms of each stress are

$$T_{11} = \lambda_1 \frac{\partial W}{\partial \lambda_1} + q, \ T_{22} = \lambda_2 \frac{\partial W}{\partial \lambda_2} + q, \ T_{33} = \lambda_1 \frac{\partial W}{\partial \lambda_3} + q. \tag{29}$$

The purpose of this model is to determine the electromechanical response of the material operating in a planar electrostriction mode, which is often measured in terms of strain in the 3-direction versus electric field. Thus, the principal stress difference between is considered,

$$T_{33} - T_{11} = \lambda_3 \frac{\partial W}{\partial \lambda_3} - \lambda_1 \frac{\partial W}{\partial \lambda_1},\tag{30}$$

Eliminating the unknown hydrostatic stress.

Eqs. (5)–(14) form the kinematic basis for the model developed in this work. In the next section, the Helmholtz free energy relating elastic to electric energy densities within the EAP is derived such that the Cauchy stresses may be determined.

3. Electromechanical response of a hyperelastic biphasic body with dipole-dipole interactions

This section outlines the methodologies for including microstructure as defined by averages of crystalline domains' relative spatial locations and orientations in to the electrostriction model. The biphasic aspect of the microstructure of PVDF-based RFE polymers is also considered through free energy contributions of each phase. It is assumed that the amorphous phase provides a hyperelastic and linear dielectric response while the crystalline phases contribute to the free energy solely through their electrostatic interactions.

3.1. Free energy formulation of a biphasic body

The strain energy density of a body composed of a crystalline and an amorphous phase is postulated as

$$W = W_{A,EI} + W_{A,LD} + W_C, \tag{31}$$

where $W_{A, El}$ and $W_{A, LD}$ are the elastic and electrostatic (linear dielectric) responses of the amorphous phase, respectively, while W_C is the dipolar response of the crystalline phase. This decomposition of the energy density function into the contributions from the amorphous phase and the crystalline phase is similar to the models developed by Richards (2010) and Zah (2014), which implemented multiple contributions into their material energy densities. The following subsections explore the separate contributions of each phase's response to the total energy density, W.

3.2. Hyperelastic response of the amorphous phase

The relaxational behavior of semicrystalline RFE polymers is due to the behavior of the amorphous phase (Ang et al., 2005; Lu, et al., 2006; Lu, et al., 2008). We assume that the amorphous phase has a hyperelastic response, which can be described by an energy density function $W_{A, El}$. Furthermore, the problem is simplified by assuming that the ellipsoidal amorphous phase of the material exhibits affine deformation, with stretch apportioning following (23), and its elastic response is governed by the eight-chain hyperelastic model by Arruda and Boyce (1993), due to its efficacy modeling polymeric materials in multiple deformation states and physical network basis. The eight-chain model, after approximation, has the form

$$W_{8ch}(I_1, \lambda_m, C_1) \approx C_1 \left[\frac{1}{2} (I_1 - 3) + \frac{1}{20\lambda_m^2} (I_1^2 - 9) + \frac{11}{1050\lambda_m^4} (I_1^3 - 27) + \frac{19}{7000\lambda_m^6} (I_1^4 - 81) + \frac{519}{673750\lambda_m^8} (I_1^5 - 243) \right],$$
(32)

where I_1 is the first principal invariant as defined in (2); C_1 and λ_m are experimentally determined constants; The constant λ_m also has a physical interpretation: it is the number of rigid links in a polymer chain.

The elastic energy must be written for only the amorphous segment of the semicrystalline element (see Fig. 4), which demands the modification of I_1 such that it represents the stretch of only the amorphous phase: $I_1^A = I_1(\lambda_A)$. As a result, we obtain $W_{8ch}(I_1^A, \lambda_m, C_1)$ for the elastic energy of the amorphous phase.

Additionally, the elastic energy density must be scaled by the volume fraction occupied by the amorphous phase, which is proportional to $(1 - v_C)$,

$$W_{AEI} = (1 - v_c)W_{8ch}(I_1^A, \lambda_m, C_1)$$
 (33)

Since the elastic energy describes the energy of our chosen differential element, we must average the energy over the entire range of orientations based on a probability density function, $f_{sc}(\phi, \theta)$. The average energy $\langle W_{A, El} \rangle$ is defined by the integral

$$\langle W_{A,El} \rangle = \frac{(1 - \nu_c)}{A_{el}} \int_0^{\pi} \int_0^{2\pi} f_{sc}(\phi, \theta) W_{8ch} \left(I_1^A(\phi, \theta), \lambda_m, C_1 \right) \sin\phi d\theta d\phi$$
(34)

The constant A_{el} is a normalizer, determined by

$$A_{el} = \int_0^{\pi} \int_0^{2\pi} f_{sc}(\phi, \theta) \sin\phi \, d\theta \, d\phi. \tag{35}$$

In the Lagrangian description, $\langle W_{A,EL} \rangle$ can also be written as (Wu and van der Giessen, 1993)

$$\langle W_{A,El} \rangle = \frac{\left(1 - \nu_c^{1/3}\right)}{A_{cl}} \int_0^{\pi} \int_0^{2\pi} f_{sc}(\Phi, \Theta) W_{8ch}(I_1^A(\Phi, \Theta), \lambda_m, C_1) sin\Phi J^{-1} d\Theta d\Phi. \tag{36}$$

We assume that the chain's orientation distribution is initially uniformly distributed, since the amorphous region exists in the same amount in every direction around the crystalline domain inside the RVE (see Fig. 3), resulting in $A_{el} = 1/4\pi$. Furthermore, the Lagrangian description of $\langle W_{A, EL} \rangle$ will be of more use to us since the initial distribution $f_{sc}(\Phi, \Theta)$ is known. However, due to the difficulty in obtaining an analytical solution to (36), we consider a discretized approach to calculating the integral in (36) numerically,

$$\langle W_{A,EI} \rangle = n \left(1 - v_c^{1/3} \right) \sum_{i}^{N_{\Theta}} \sum_{j}^{N_{\Phi}} f_{sc} \left(\Phi_j, \Theta_i \right) W_{8ch} \left(I_1^A \left(\Phi_j, \Theta_i \right), \lambda_m, C_1 \right) sin \Phi J^{-1} \Delta \Theta \Delta \Phi, \tag{37}$$

where $\Delta\Theta$ and $\Delta\Phi$ are step sizes for the angles, and N_{Θ} and N_{Φ} are the total number of steps, which are related to the step sizes by $N_{\Theta}\Delta\Theta=2\pi$ and $N_{\Theta}\Delta\Phi=\pi$.

3.3. Linear dielectric response of the amorphous phase

Following Capsal et al. (2012), the amorphous phase comprises chain structures that generate a linear dielectric response. Its saturation field is very high, but its dielectric constant (approx. 1–5) is significantly lower than the effective dielectric constant produced by the crystalline phases (approx. 50 or greater), as discussed in Capsal et al. (2012).

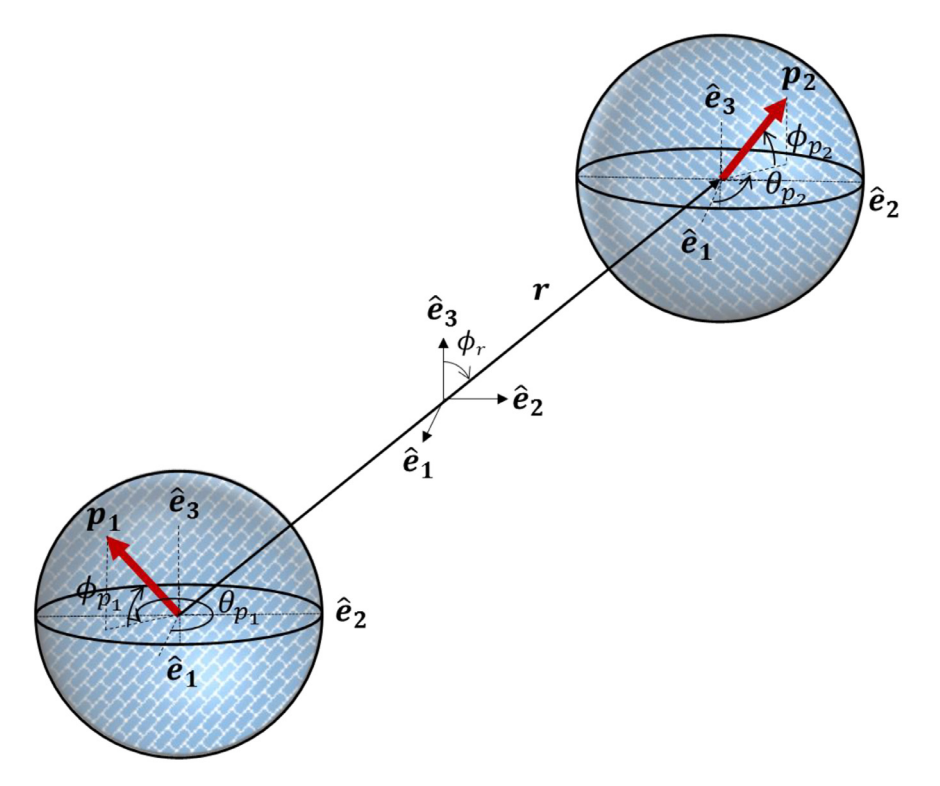


Fig. 5. Variables defining the orientations and separation of two dipole moments with respect to the basis vector \hat{e}_3 . The angles calculated in Eq. (68) are visually depicted at relevant locations; α_1 is drawn separately for simplicity.

The linear dielectric energy density of the amorphous phase can be written as

$$W_{A,LD} = (1 - \nu_c) \frac{J}{2} \epsilon_r \epsilon_0 (\mathbf{E} \cdot \mathbf{E}), \tag{38}$$

where ϵ_r is the relative electric permittivity of the amorphous phase, ϵ_0 is the electric permittivity of free space, and \boldsymbol{E} is the applied field. The form of (37) is a common representation of a linear dielectric material response, scaled by the volume fraction of the amorphous phase, $(1 - \nu_c)$.

3.4. Dipole-dipole interactions of crystalline phases

As noted in Section 1.2, relative spatial and orientation characteristics of dipolar domains are important to their energetic contributions and subsequent electro-mechanical coupling. Consequently, the work herein seeks to develop a model framework that incorporates those dependencies. The model framework begins with a statement of the interaction energy (Duan et al., 2004) between two crystalline domains, treated as nominally point dipoles of dipole moments p_1 and p_2 , as shown in Fig. 5. The energy is in the form of

$$U_d = \frac{1}{4\pi\epsilon} \left[\frac{\mathbf{p}_1 \cdot \mathbf{p}_2}{r^3} - \frac{3(\mathbf{p}_1 \cdot \mathbf{r})(\mathbf{p}_2 \cdot \mathbf{r})}{r^5} \right]. \tag{39}$$

where r is the dipole-dipole separation vector with a magnitude of r, and ϵ is the electric permittivity of the medium that contains the dipoles. This permittivity, ϵ , should not be confused with the overall permittivity of the polymer; it is strictly the permittivity of the space—or medium—between the dipoles.

The free energy of the crystalline domains is assumed comprised wholly of the potential between dipoles. Consequently, the energy density of the crystalline domain W_C can be written as

$$W_C = \frac{1}{V_c} U_d. \tag{40}$$

where the volume of the crystalline phase is $V_c = v_c V_{tot}$. Specifically, (40) characterizes the attractive or repulsive potentials between a pair of crystalline domains, associated with Ω_{C_i} . This dipole energy will be coupled to the elastic energy, which characterizes the elastic potential of the amorphous domains, Ω_A , in a representative volume element to derive the total free energy density.

For a convenient assessment of the electromechanical strains, the dipolar energy density can be written in terms of \mathbf{F} by substituting the kinematic relationships in (11) and (12) and the definition of the interaction energy in (39), into (40), yielding

$$\tilde{W}_C = \frac{1}{4\pi X_c V_{tot} \epsilon} \left[\frac{\mathbf{p}_1 \cdot \mathbf{p}_2}{[\mathbf{F}\mathbf{R} \cdot \mathbf{F}\mathbf{R}]^{3/2}} - \frac{3(\mathbf{p}_1 \cdot \mathbf{F}\mathbf{R})(\mathbf{p}_2 \cdot \mathbf{F}\mathbf{R})}{[\mathbf{F}\mathbf{R} \cdot \mathbf{F}\mathbf{R}]^{5/2}} \right]. \tag{41}$$

Finally, the total energy density of the material is rewritten by combining (37) and (41),

$$\tilde{W} = \frac{\left(1 - X_{C}^{1/3}\right)}{A_{el}} \sum_{i}^{N_{\Theta}} \sum_{j}^{N_{\Phi}} f_{sc}\left(\Phi_{j}, \Theta_{i}\right) W_{8ch}\left(I_{1}^{A}\left(\Phi_{j}, \Theta_{i}\right), \lambda_{m}, C_{1}\right) \sin\Phi J^{-1} \Delta\Theta \Delta\Phi + (1 - X_{C}) \frac{J}{2} \epsilon_{r} \epsilon_{0}(\mathbf{E} \cdot \mathbf{E}) + \frac{1}{4\pi X_{c} V_{tot} \epsilon} \left[\frac{\mathbf{p}_{1} \cdot \mathbf{p}_{2}}{[\mathbf{F}\mathbf{R} \cdot \mathbf{F}\mathbf{R}]^{3/2}} - \frac{3(\mathbf{p}_{1} \cdot \mathbf{F}\mathbf{R})(\mathbf{p}_{2} \cdot \mathbf{F}\mathbf{R})}{[\mathbf{F}\mathbf{R} \cdot \mathbf{F}\mathbf{R}]^{5/2}} \right].$$
(42)

4. Orientation dependence of polarization of crystalline domains

4.1. Determining magnitude of the average dipole moment

When subject to an external field, the crystalline domains, Ω_i , comprise collinear electric dipoles resulting in a net dipole moment p per crystalline domain. We assume that each crystalline domain exhibits an average dipole moment strength, p. It is convenient to write the dipole moment of a crystalline domain as

$$\mathbf{p} = p\hat{\mathbf{p}} \tag{43}$$

where the dipole moment vector is split into its magnitude p and the orientation component, \hat{p} , which is the unit vector defined as

$$\hat{\mathbf{p}} = \cos \theta_p \sin \phi_p \hat{\mathbf{e}}_1 + \sin \theta_p \sin \phi_p \hat{\mathbf{e}}_2 + \cos \phi_p \hat{\mathbf{e}}_3 \tag{44}$$

where θ_p and ϕ_p are new polar and azimuthal angles defined for the dipole moment vector with respect to the orthonormal basis vectors, as shown in Fig. 5.

When considering the alignment of dipoles, the angle ϕ_p is of interest, as it defines the alignment of the dipole with respect to the direction of the applied field, prescribed as \hat{e}_3 . This angle can be better visualized in Fig. 5, which depicts two dipoles separated by some vector \mathbf{r} , each assigned ϕ_{pi} .

The average dipole moment magnitude p can be determined by assessing the polarization of a representative volume element (RVE) under the saturation condition, $E \to \infty$, which implies $\lim_{E \to \infty} P \to P_{sat}$, where P_{sat} is the saturated electric polarization density. Assuming that all crystalline domains will perfectly align at some saturation field strength, at saturation the dipole moment magnitude p can be nominally expressed as

$$p = \frac{V_{tot} P_{sat}}{N},\tag{45}$$

in which N is the number of dipoles (i.e., crystalline domains) within the RVE of volume V_{tot} . Note that P_{sat} is a directly measurable quantity.

Substitution of (44) and (45) in (43) yields,

$$\boldsymbol{p} = \frac{V_{tot}P_{sat}}{N} \left(\cos\theta_p \sin\phi_p \hat{\boldsymbol{e}}_1 + \sin\theta_p \sin\phi_p \hat{\boldsymbol{e}}_2 + \cos\phi_p \hat{\boldsymbol{e}}_3\right). \tag{46}$$

4.2. Dipole moment orientations based on a probability distribution function

This subsection introduces the concept of polar domain orientations as a function of electric field. This relationship is characterized by a von Mises distribution function incorporating previous descriptions of the average orientation of dipoles to derive an expression for a probability distribution function (PDF) of polar domain orientations that is a function of the applied electric field, *E*.

The dipole-dipole energy in (39) is influenced by crystalline domains alignments with respect to the field, and with respect to each other. The alignment of a set of crystalline domains can be described by a distribution function, denoted by f_{ϕ_p} , through which we can determine the relationship between the applied electric field and the average alignment of crystalline domains. The alignment is quantified by ω , as defined in Fig. 5, which assumes rotational symmetry about \hat{e}_3 (an artifact of assuming in-plane isotropy). The angle is defined in this manner for convenience in later calculations.

We consider the collection of crystalline domains with net dipoles p, of uniform strength, p, with varying orientations about the axis \hat{e}_3 , defined by ϕ_p in (44) (see Figs. 2 and 5). For the set of dipoles, the average dipole moment can be expressed as

$$\langle \mathbf{p} \rangle = \langle p \hat{\mathbf{p}} \rangle \tag{47}$$

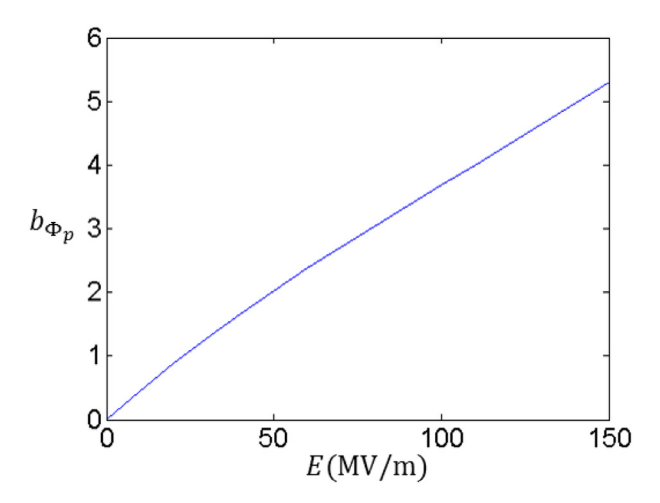


Fig. 6. Relationship between ϕ_p and E as calculated by (51).

In (47), the brackets $\langle \, \cdot \, \rangle$ denote the average over all dipoles.

The average orientation of the dipoles with respect to \hat{e}_3 based on a probability distribution function is adopted as

$$\langle \cos \phi_p \rangle = \frac{1}{A_{\phi_p}} \int_{-\pi}^{\pi} f_{\phi_p} (\phi_p | \mu, b_{\phi_p}) \cos \phi_p d\phi_p, \tag{48}$$

where $f_{\phi_p}(\phi_p|~\mu,b_{\phi_p})$ denotes a von Mises (wrapped normal) distribution, with the form

$$f_{\phi_p}(\phi_p | \mu, b_{\phi_p}) = \frac{e^{b_{\phi_p}\cos(\phi_p - \mu_{\phi_p})}}{2\pi I_0(b_{\phi_p})},\tag{49}$$

in which $\phi_p \in [-\pi, +\pi]$, while μ_{ϕ_p} is the mean of the distribution, I_0 is the modified Bessel function of the first kind with order 0, and b_{ϕ_p} is the concentration parameter that determines the width of the distribution of dipole orientations about the mean μ_{ϕ_p} . The term A_{ϕ_p} normalizes the distribution and can be computed by equating the integral of $f_{\phi_p}(\phi_p|\mu,b_{\phi_p})d\phi_p$ over the domain of interest to unity. In this context, we emphasize that this distribution of dipole orientations refers to the distribution of dipole orientations of the crystalline domains, Ω_i . Each crystalline domain is treated as a single dipole. With this distinction in mind, the dipoles—or crystal domains—are assumed to perfectly align with the field along $\hat{\mathbf{e}}_3$ (given $\mathbf{E} = E\hat{\mathbf{e}}_3$) as $E \to \infty$, so the mean of the distribution in (49) is set to $\mu_{\phi_p} = 0$. It is possible that variable processing or loading conditions may in the future warrant $\mu_{\phi_p} \neq 0$.

The utility of the distribution function lies in its statistical representation of a set of domains that gradually align with an external field. The distribution's concentration, b_{ϕ_p} , couples the effect of the external field to the change in alignment of the crystalline domains. Without influence of an electric field, it is assumed that crystalline domains exist in a randomly oriented state characterized by $b_{\phi_p}=0$. A uniform distribution of dipole orientations falls in a full circular range, such that there is an equal probability of a dipole within the collection to be at any orientation between $\phi_p=-\pi$ and $\phi_p=+\pi$. By contrast, a higher value such as $b_{\phi_p}=5$ means there is a much greater probability of dipole orientations near the mean alignment μ_{ϕ_p} . To determine the relationship between electric field and the concentration parameter, we consider the averaging method for dipole orientations found in the appendix of Capsal et al (2012), in which the average dipole orientation $\langle\cos\phi_p\rangle$ is expressed as

$$\langle \cos \phi_p \rangle = \coth \left[\frac{E}{E_s} \right] - \frac{E_s}{E}. \tag{50}$$

Thus, combining (48)-(50) yields

$$\coth\left[\frac{E}{E_s}\right] - \frac{E_S}{E} = \frac{1}{A_f} \int_0^{\pi} \frac{e^{b_{\phi_p}\cos(\phi_p - \mu_{\phi_p})}}{2\pi I_0(b_{\phi_p})} \cos\phi_p d\phi_p,\tag{51}$$

which can be used to evaluate b_{ϕ_p} as a function of the experimentally applied electric field strength E by seeking successive $[E, b_{\phi_p}]$ pairs that satisfy (51), to within a given tolerance, for an experimentally determined constant, E_s . (Note: E_s is not the field at which saturation occurs, but the field when the polarization response breaks from a linear regime. Consequently, a typical RFE polymer will not saturate until far beyond E_s . This notation is adopted to stay consistent with Capsal et al., 2012.) The correlation between E_s and E_s is shown in Fig. 6.

The correlation between E and b_{ϕ_p} is shown in Fig. 6. Fig. 7 illustrates the relationship between E and b_{ϕ_p} with a plot of the distribution in (49) at varying electric field strengths. As E increases, the probability of alignment increases near $\phi_p = 0$, the direction of E.

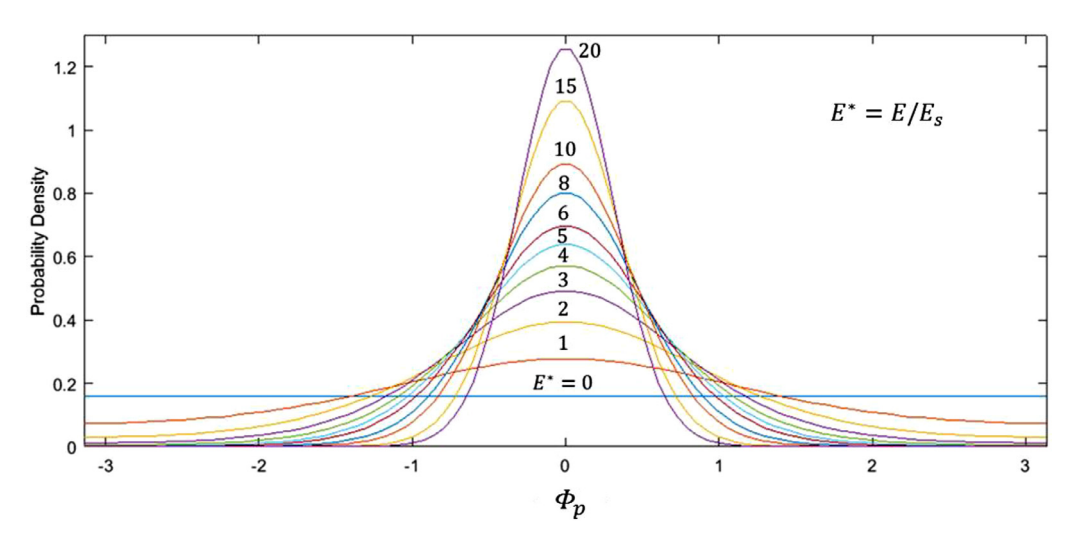


Fig. 7. A von Mises distribution function is chosen as the PDF of the electric dipoles. With the implementation of $b_{\phi_p} = b_{\phi_p}(E)$ solved in (51), the model represents a set of dipoles progressively aligning with the field direction ($\phi_p = 0$) as E is increased.

The purpose of deriving the $[E,b_{\phi_p}]$ pairs is to utilize them in assessing the average of the dot products, $\langle \pmb{p}_1 \cdot \pmb{p}_2 \rangle$, in the interaction energy, (41). One approach to calculating $\langle \pmb{p}_1 \cdot \pmb{p}_2 \rangle$ is by determining the average angle of the dipoles $\langle \pmb{\phi}_p \rangle$ with respect to the field such that the average dipole moment unit vector $\langle \hat{\pmb{p}} \rangle$ is written as

$$\langle \hat{\mathbf{p}} \rangle = \cos \theta_p \sin \phi_p \hat{\mathbf{e}}_1 + \sin \theta_p \sin \phi_p \hat{\mathbf{e}}_2 + \cos \phi_p \hat{\mathbf{e}}_3, \tag{52}$$

where $\langle \theta_p \rangle$ is the average angle based on a uniform distribution $f_{\theta_p}(\theta_p | \mu_{\theta_p} = 0, b_{\theta_p} = 0)$, and $\langle \phi_p \rangle$ is calculated by applying the $[E, b_{\phi_p}]$ pairs determined by (51) into

$$\langle \phi_p \rangle = \frac{1}{A_{\phi_p}} \int_0^{\pi} f_{\phi_p} (\phi_p | \mu_{\phi_p}, b_{\phi_p}(E)) \phi_p d\phi_p, \tag{53}$$

and similarly

$$\langle \theta_p \rangle = \frac{1}{A_{\theta_p}} \int_0^{\pi} f_{\theta_p} (\theta_p | \mu_{\theta_p} = 0, b_{\theta_p} = 0) \theta_p d\theta_p, \tag{54}$$

in which A_{ϕ_p} and A_{θ_p} normalize the integrals over the domain.

The form of $\langle \hat{\pmb{p}} \rangle$ incorporated into the first term of (41) reduces to $\langle \hat{\pmb{p}} \rangle \cdot \langle \hat{\pmb{p}} \rangle = 1$, which may not always be true, because crystalline domains are not assumed collinear with each other. Alternatively, we can determine the average dot product $\langle \hat{\pmb{p}} \cdot \hat{\pmb{p}} \rangle$, by discretely sampling two sets of angles, $\{\phi_{p1}, \theta_{p1}\}$ and $\{\phi_{p2}, \theta_{p2}\}$, based on the distributions (53) and (54), utilizing a von Mises distribution function in (49), and evaluating at $[E, b_{\theta_p}]$ pairs. The sets of angles yields two sets of dipole moment directions, $\{\hat{\pmb{p}}_1\}$ and $\{\hat{\pmb{p}}_2\}$, such that the average dot product $\langle \hat{\pmb{p}} \cdot \hat{\pmb{p}} \rangle$ can be evaluated by

$$\langle \hat{\boldsymbol{p}}_1 \cdot \hat{\boldsymbol{p}}_2 \rangle = \frac{1}{N_p} \sum_{k=1}^{N_p} \left\{ \hat{\boldsymbol{p}}_1 \right\}_k \cdot \left\{ \hat{\boldsymbol{p}}_2 \right\}_k. \tag{55}$$

Similarly, the average dot products $\langle \hat{\pmb{p}}_1 \cdot \hat{\pmb{r}} \rangle$ and $\langle \hat{\pmb{p}}_2 \cdot \hat{\pmb{r}} \rangle$ can be calculated by

$$\langle \hat{\boldsymbol{p}}_1 \cdot \hat{\boldsymbol{r}} \rangle = \frac{1}{N_p} \sum_{k=1}^{N_p} \left\{ \hat{\boldsymbol{p}}_1 \right\}_k \cdot \hat{\boldsymbol{r}}, \tag{56}$$

$$\left\langle \hat{\boldsymbol{p}}_{2} \cdot \hat{\boldsymbol{r}} \right\rangle = \frac{1}{N_{p}} \sum_{k=1}^{N_{p}} \left\{ \hat{\boldsymbol{p}}_{2} \right\}_{k} \cdot \hat{\boldsymbol{r}} \tag{57}$$

The sample size N_p is studied more in the next section. It is noted that the expressions (55)–(57) provide a means of estimating the required dot products and carry the assumption that the magnitudes of crystalline domains, p, are uniform across all crystallites, which places variance of (47) into \hat{p} , where $p = \langle p \hat{p} \rangle$. As a result,

$$W_{C} = \frac{p^{2}}{4\pi X_{c} V_{tot} \epsilon r^{3}} \left[\langle \hat{\boldsymbol{p}}_{1} \cdot \hat{\boldsymbol{p}}_{2} \rangle - 3 \langle \hat{\boldsymbol{p}}_{1} \cdot \hat{\boldsymbol{r}} \rangle \langle \hat{\boldsymbol{p}}_{2} \cdot \hat{\boldsymbol{r}} \rangle \right]. \tag{58}$$

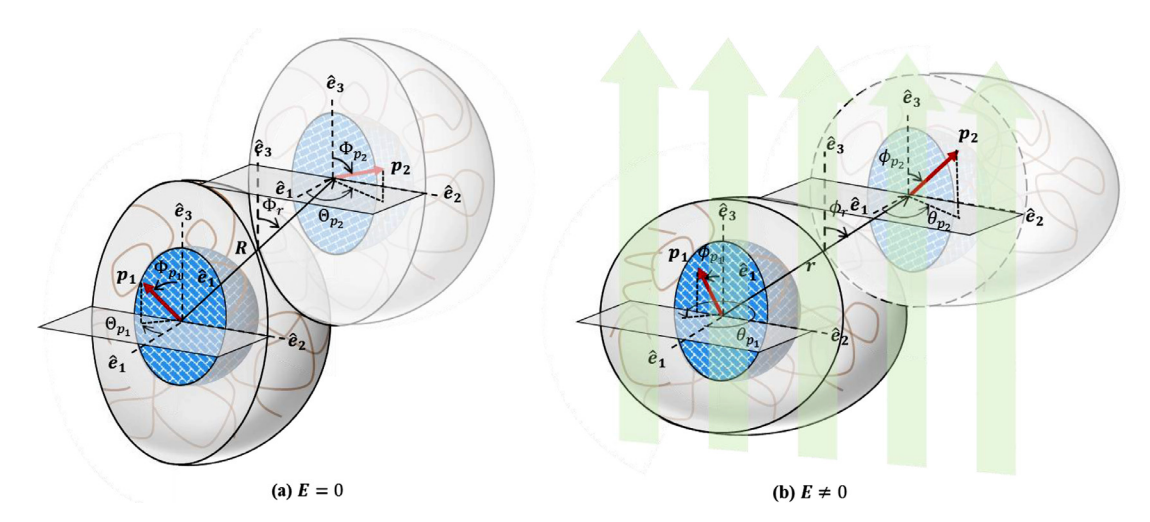


Fig. 8. The RVE is represented by a sphere annotated with quantities with a subscript of 1, while a neighboring RVE is indicated by the second sphere annotated with quantities with subscript 2. Depiction of spheres in (a) represent the undeformed shapes of the RVE and neighboring body with no field present, at an initial relative orientation of crystallites defined, and (b) illustrates the deformed shapes of the RVE and neighboring body under an applied field along \hat{e}_3 , creating nominal \hat{e}_3 -alignment and dipole-dipole forces, and subsequent uniaxial compression of the RVE. Please note that the neighboring RVE display does not represent a spherical contact problem.

5. Formulation of electrostrictive model for different network models

5.1. Derivation of the discrete network model response under a principle deformation mode

In this subsection, we consider the interaction of the RVE with neighboring crystalline domains to study the coupling of the dipole-dipole forces between crystalline domains with the hyperelasticity of the amorphous phase within the RVE. Consider the chosen single-crystallite RVE (see Fig. 3), which represents any chosen semicrystalline region in the material. The crystalline domain in this RVE, which we assume behaves as a rigid polarizable region (whose dipole moment is treated as a point dipole located at its center), experiences interactions with neighboring dipoles. To represent the dipole-dipole interaction effect of the nearest neighbor crystalline domains on the RVE, we draw a second body containing another crystalline domain at an arbitrary orientation Φ_r from the RVE's center point, as shown in Fig. 8. The second body is shown more transparent because we are only considering its interaction effects on the main RVE. It should be noted that the ellipsoidal volumes are meant to give geometric definition to the regions of influence of any given crystallite dipole. Consequently, the deformation of these volumes is imposed with respect to the macroscopic deformation gradient, and not, as the figure might suggest, spherical contact mechanics. The interaction energy of the dipoles induces deformation over the affected volumes that produces strain energy within their amorphous phases in balance with the dipole energy. Additionally, it should be noted that the bodies are cut to better show the angles associated with the dipole moments of each crystalline domain. We further assume that all crystalline domains are separated by the same distance $R = 2R_{RVE}$, which allows us to conveniently adopt (41) without any changes in notation. The initial case we study is a fixed Φ_r ($\Phi_r = const.$), referred to as the discrete network model, which will allow us to determine the effects of relative spatial locations of the nearest crystalline domains on the RVE. Later adaptations of this framework will provide means of more complex network averaging schemes over a range of Φ_r .

The representative volume element (RVE) is assumed spherical, initially, and incompressible, such that the nominally constant volume can be written as

$$V_{RVE} = \frac{4}{3I}\pi \left(R_{RVE}\right)^3,\tag{59}$$

where the Jacobian I is defined in (62).

Given the analysis of this paper focuses on electrostriction, the semicrystalline body is assumed to undergo affine deformation in the principle space, for which the deformation gradient holds the form

$$\mathbf{F} = \begin{pmatrix} \lambda_1 & 0 & 0 \\ 0 & \lambda_2 & 0 \\ 0 & 0 & \lambda_3 \end{pmatrix},\tag{60}$$

As shown in Fig. 8, the network model is defined within a Cartesian coordinate system with basis vectors $\{\hat{e}_1, \hat{e}_2, \hat{e}_3\}$ and two spherical coordinate systems with coordinates $\{R, \Theta, \Phi\}$ and $\{r, \theta, \phi\}$ in the undeformed and deformed configurations, respectively. These coordinates allow for more convenient derivations of the energy of the network model.

Maintaining the assumption of uniaxial deformation, the magnitude of the vector \mathbf{r} between the two dipoles in Fig. 8 can be written in terms of the spherical coordinate system as

$$\mathbf{r} = R(\lambda_1 \cos \Theta_r \sin \Phi_r \hat{\mathbf{e}}_1 + \lambda_2 \sin \Theta_r \sin \Phi_r \hat{\mathbf{e}}_2 + \lambda_3 \cos \Phi_r \hat{\mathbf{e}}_3) \tag{61}$$

where the principle stretch terms λ_i correspond to each principle direction. The common incompressibility assumption is made, so that I = 1, where I is the Jacobian defined as

$$J = det \mathbf{F}. \tag{62}$$

Consequently,

$$J = \lambda_1 \lambda_2 \lambda_3 = 1 . \tag{63}$$

Typically, electrostriction is measured in terms of the applied field versus strain in the direction of the field, which is conventionally the 3-direction. To comply with existing measures, we set $E = E\hat{e}_3$, and put focus on λ_3 . We assume that the directions transverse to the direction of polarization will experience equivalent electromechanical strain, i.e., the principal electrostriction in-plane is isotropic. The resulting stretch dependences can be written as

$$\lambda_1 = \lambda_2 = \lambda_3^{-\frac{1}{2}}.\tag{64}$$

Substitution of (64) into (61) yields a stretch dependent expression for the deformed radius magnitude, r, namely

$$r = R\sqrt{\lambda_3^{-1} \sin^2 \Phi_r + \lambda_3^2 \cos^2 \Phi_r}. (65)$$

We can also consider rewriting λ_A for the electrostriction case, utilizing (64), which reduces (8) to

$$\lambda_{A} = \frac{1}{(1 - \nu_{c})} \sqrt{\left(\sin^{2}\Phi\right) \lambda_{3}^{-1} + \left(\cos^{2}\Phi\right) \lambda_{3}^{2}} - \frac{\nu_{c}}{(1 - \nu_{c})}$$
(66)

Additionally, the constitutive relation in (30) can be written in terms of λ_3 by substitution of (64). This form is amenable to the determination of electrostrictive response, E vs. λ_3 and given by

$$\frac{\partial W}{\partial \lambda_3} = 0. ag{67}$$

The substitution of $R = 2R_{RVE}$, dipole moment magnitude (45), N = 1 (for one crystalline domain in RVE), and the radius (65) into the energy in (58), yields

$$W_{C} = \frac{P_{Sat}^{2}}{3\nu_{c}\epsilon \left(\lambda_{3}^{-1}\sin^{2}\Phi_{r} + \lambda_{3}^{2}\cos^{2}\Phi_{r}\right)^{3/2}} \left[\left\langle \hat{\boldsymbol{p}}_{1} \cdot \hat{\boldsymbol{p}}_{2} \right\rangle - 3\left\langle \hat{\boldsymbol{p}}_{1} \cdot \hat{\boldsymbol{r}} \right\rangle \left\langle \hat{\boldsymbol{p}}_{2} \cdot \hat{\boldsymbol{r}} \right\rangle \right]. \tag{68}$$

For simplicity, we will drop the subscript on λ_3 such that $\lambda_3 = \lambda$. The dot products in (68) are averages determined by the sampling from the von Mises distribution ($N_\omega = 10^5$) in (49)–(51), and the orientation Φ_r . Upon substitutions made into (68), and the resulting simplifications, W_C becomes independent of R and R_{RVE} , allowing us to isolate the influences of only orientation components of the dipole positions when calculating electrostriction. Consequently, this RVE structure will suffice for the purpose of this study.

The elastic energy can also be simplified for the electrostriction case. The local invariant, in its general form $I_1^A = (\lambda_1^A)^2 + (\lambda_2^A)^2 + (\lambda_3^A)^2$, can be written as $I_1^A = (2\lambda_3^A)^{-1} + (\lambda_3^A)^2$, in which λ_i^A are the principal stretches of just the amorphous region, as defined in (27). With the substitution for I_1^A , the total energy can be written,

$$\tilde{W} = \frac{(1 - \nu_c)}{A_{el}} \sum_{i}^{N_{\Theta}} \sum_{j}^{N_{\Phi}} f_{sc}(\Phi_j, \Theta_i) W_{8ch}(I_1^A(\lambda, \Phi_j, \Theta_i), \lambda_m, C_1) sin\Phi \Delta \Theta \Delta \Phi + (1 - \nu_c) \frac{\lambda^{-2}}{2} \epsilon_r \epsilon_0(\mathbf{E} \cdot \mathbf{E})
+ \frac{P_{sat}^2}{3\nu_c \epsilon (\lambda^{-1} sin^2 \Phi_r + \lambda^2 cos^2 \Phi_r)^{3/2}} [\langle \hat{\mathbf{p}}_1 \cdot \hat{\mathbf{p}}_2 \rangle - 3\langle \hat{\mathbf{p}}_1 \cdot \hat{\mathbf{r}} \rangle \langle \hat{\mathbf{p}}_2 \cdot \hat{\mathbf{r}} \rangle]$$
(69)

5.2. Analysis of the response of two cases of the discrete network model

Two limiting cases emerge from the arbitrarily oriented discrete network model shown in Fig. 8: the parallel, \parallel , and perpendicular, \perp , discrete neighboring crystallite locations. These cases derive their names from the neighboring RVE's orientation with respect to the applied field. Hence, the parallel discrete network model consists of crystalline domains oriented parallel to E, and the perpendicular case assumes neighboring crystalline domains to exist perpendicular with respect to E. These two specific cases of the discrete network model are illustrated in Fig. 9.

The significance of the two specific discrete network cases is apparent from the behavior of W_C , which is based on dipole-dipole interactions. The energy (68) is a function of the direction of \mathbf{r} , and the orientations of \mathbf{p}_1 and \mathbf{p}_2 . The energy can be reduced in each special case as $E \to \infty$, yielding

$$\lim_{E \to \infty} \bar{W}_{C,\parallel} = -\left(\frac{2P_s^2}{3\nu_c \epsilon}\right) \lambda^{-3},\tag{70}$$

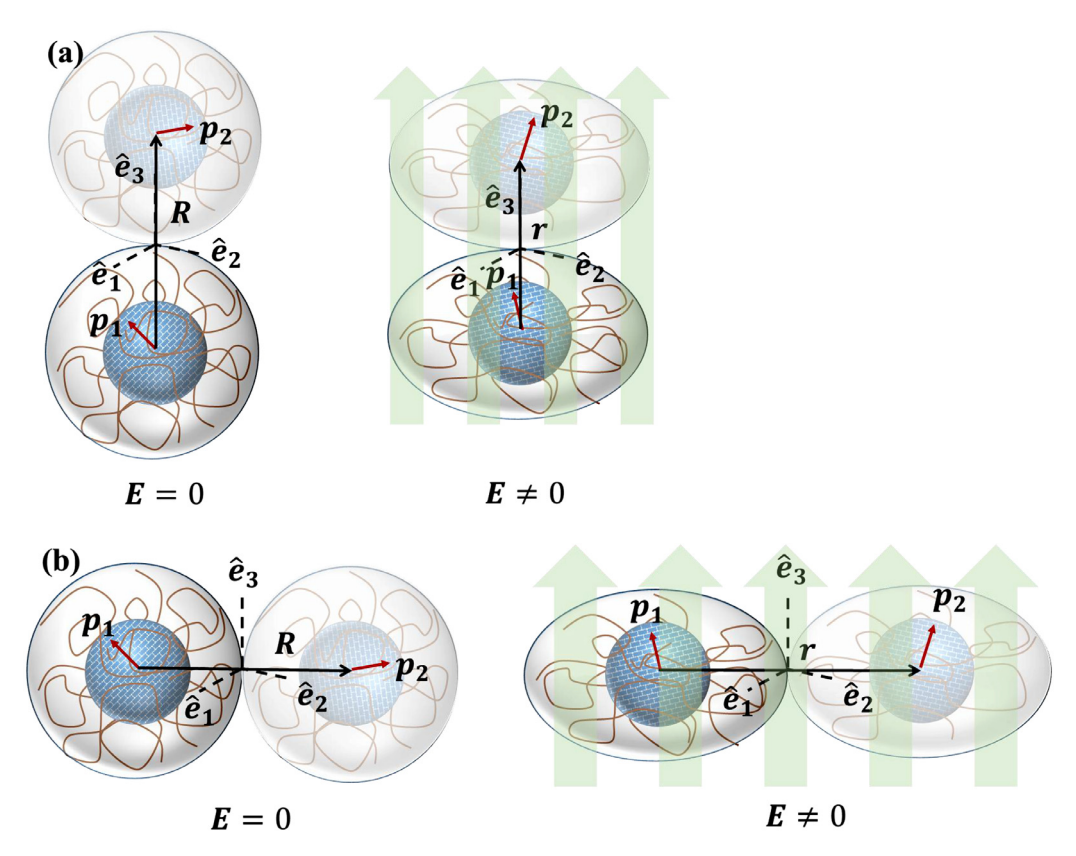


Fig. 9. The discrete network model is shown for two specific cases. The parallel case is shown in (a), where the vector to nearest neighboring crystalline domain, **r**, is parallel to the external field, while in the perpendicular case in (b) **r** is perpendicular to the external field.

And

$$\lim_{E \to \infty} \bar{W}_{C,\perp} = \left(\frac{P_s^2}{3\nu_c \epsilon}\right) \lambda^{3/2} \ . \tag{71}$$

To gain a better understanding of the geometry-dependent qualitative differences between the two limiting cases of the discrete network model, we non-dimensionalize each subcase's energy function by the constant $P_s^2/(3X_C\epsilon)$ leaving

$$W_{\mathcal{C}}^* = W_{\mathcal{C}} \left(\frac{P_{\mathcal{S}}^2}{3\nu_{\mathcal{C}} \epsilon} \right)^{-1} \tag{72}$$

In (72), the asterisk on W_C denotes its non-dimensionalized property. The limit of the parallel and perpendicular single chain network models as $E \to \infty$ are expressed below in (73) and (74), respectively.

$$\lim_{E \to \infty} \bar{W}_{C,\parallel}^* = -2\lambda^{-3} \tag{73}$$

$$\lim_{E \to \infty} \bar{W}_{C,\perp}^* = \lambda^{3/2} \tag{74}$$

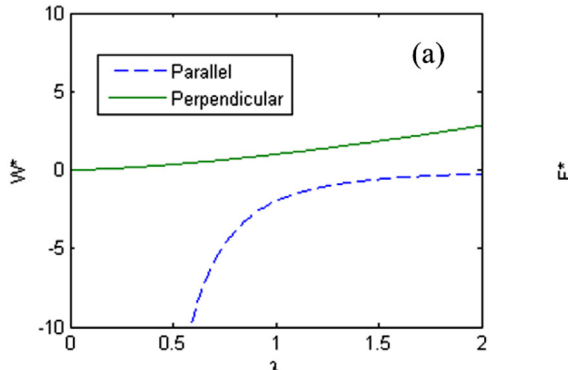
These energies are compared in Fig. 10a as functions of λ , both exhibiting an increase in energy as λ increases. Due to the coefficients in (73) and (74), the parallel case is greater in magnitude by a factor of 2 than the energy of the perpendicular case at $\lambda=1$ (as shown in Fig. 10a), and the rate of change of the parallel case is higher below $\lambda=1$ due to the higher order exponential on λ in (73) compared to (74). Furthermore, the signs of (73) and (74) are opposite, which implies that in the transition between the two extreme cases, there is a state of orientation that generates zero interaction energy.

The stress generated by the interaction energy of the dipoles can be determined by

$$T_{\mathcal{C}}^* = \frac{\partial W^*_{\mathcal{C}}}{\partial \lambda}.\tag{75}$$

With (75), the forces corresponding to the two cases of the single chain network model are shown in (76) and (77),

$$\lim_{E \to \infty} T_{C,\parallel}^* = 6\lambda^{-4} \tag{76}$$



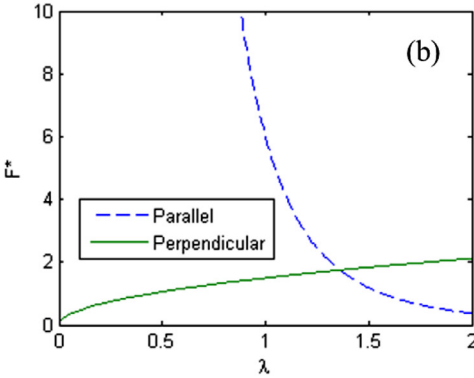


Fig. 10. The non-dimensionalized energies (a) and the corresponding forces (b) of the two cases of the single chain network model, parallel and perpendicular, are plotted versus the stretch in the direction of the applied electric field. The comparisons highlight key differences in the strengths of the interactive energies/forces between the parallel and perpendicular cases.

$$\lim_{E \to \infty} T_{C,\perp}^* = \frac{3}{2} \lambda^{1/2}. \tag{77}$$

These dipolar stresses are plotted in Fig. 10b. There are significant differences between (76) and (77): firstly, the parallel case, (76), has a coefficient of 6, while the perpendicular case, (77), has a coefficient of 3/2. Thus, when $\lambda=1$ and $E\to\infty$, the ratio of $T^*_{C,\parallel}:T^*_{C,\perp}$, is 4:1. In addition, the fourth-order exponent on λ in (76) results in a quartic increase as $\lambda\to 0$, while the exponent in (77) is 1/2. Consequently, as $\lambda\to 0$, the ratio of the forces, $T^*_{C,\parallel}:T^*_{C,\perp}$ diverges towards ∞ .

In comparison, the dielectric energy of the amorphous phase, under the incompressibility assumption and $\mathbf{E} = E\hat{\mathbf{e}}_3$, can be simplified to

$$W_{A,DE} = (1 - v_c) \frac{\lambda_3^{-2}}{2} \epsilon_r \epsilon_0 E_3^2$$
 (78)

The stress generated by the amorphous phase's dielectric response can also be defined,

$$T_{A,DE} = \frac{\partial W_{A,DE}}{\partial \lambda_3} = \lambda_3^{-3} \epsilon_r \epsilon_0 E_3^2 \tag{79}$$

Recall that the dielectric constant of the amorphous phase ϵ_r is relatively low: approximately between 1 and 5 (Capsal et al., 2012). At low fields, when $E_3 \sim 10^6 \, V/m$, the order of magnitude of the amorphous phase's dielectric contribution is $\sigma_{A, DE} \sim 10$. At high fields, when $E_3 \sim 10^8 \, V/m$, $\sigma_{A, DE} \sim 10^4$.

In contrast, the crystalline phase's dielectric response is driven by dipole-dipole interactions. The parallel and perpendicular spatial alignment cases are considered for the dipole-based energy, which yield the stresses,

$$T_{C,\parallel} = \frac{P_s^2 \lambda^{-4}}{\nu_c \epsilon_r \epsilon_0} F(E),$$

$$T_{C,\perp} = \frac{P_s^2 \lambda^{3/2}}{2\nu_c \epsilon_r \epsilon_0} F(E),$$
(80)

The function F(E) contains the Langevin orientation model (found in second term of Eq. 33) and determines the dot products of the dipole moment, and separation vectors. The output of F(E) varies between 0 and 1 for the perpendicular case, and 0 and 2 for the parallel case; furthermore, due to a relatively low field saturation of the crystalline phase, the contributions of the crystalline regions will quickly reach their maximum values within the typical range of applied field in experiments, which is between 0 and 150 MV/m. Consequently, the magnitudes of the crystalline phase's forces (at non-extreme λ values; i.e, $\lambda \sim 1$) are largely determined by the order of magnitude of $P_s^2/(\nu_c\epsilon_r\epsilon_0)$, which is 10^9 if $P_s^2 \sim 10^{-2}$ C/m^2 , $\epsilon_r\epsilon_0 \sim 10^{-12}$ F/m, and $\nu_c \sim 10^{-1}$. Thus, dipolar stresses generated by the crystalline phase will achieve stress on the order of 10^9 Pa near saturation (i.e., $150 \, \text{MV/m}$).

Due to its relatively small stress generation with respect to the crystalline phases, the dielectric contribution of the amorphous phase can be ignored within the ranges that will be analyzed in this study.

Consequently, the non-dimensionalization of the coupled response can be calculated by the traction-free equilibrium of only the crystalline phase's dipolar response and the amorphous phase's elastic response. Enforcing equilibrium $\frac{dW_C^*}{\partial \lambda} + \frac{dW_{A,El}^*}{\partial \lambda} = 0$, results in

$$\frac{\partial W_{A,El}^*}{\partial \lambda_3} = -H\left(\frac{\partial W_C^*}{\partial \lambda_3}\right). \tag{81}$$

where the parameter H is a combination of model parameters defined as $H = P_{Sat}^2/(3C_1v_c\epsilon)$, and the energy $W_{A,El}^*$ is a result of non-dimensionalization, $W_{A,El}^* = W_{A,El}/C_1$. Accordingly, the forms of both sides of (81) may be determined by substituting the dipolar energy, (68), and the elastic energy in (37), into (81), yielding

$$\frac{(1 - \nu_c)}{A_{el}} \sum_{i}^{N_{\Theta}} \sum_{j}^{N_{\Phi}} f_{sc}(\Phi_j, \Theta_i) W^*_{8ch}(I_1^A(\lambda, \Phi_j, \Theta_i), \lambda_m) sin\Phi \Delta \Theta \Delta \Phi$$

$$= -H \frac{\partial}{\partial \lambda_2} \left[(\lambda^{-1} sin^2 \Phi + \lambda^2 cos^2 \Phi)^{-\frac{3}{2}} \right] (\langle \hat{\boldsymbol{p}}_1 \cdot \hat{\boldsymbol{p}}_2 \rangle - 3 \langle \hat{\boldsymbol{p}}_1 \cdot \hat{\boldsymbol{r}} \rangle \langle \hat{\boldsymbol{p}}_2 \cdot \hat{\boldsymbol{r}} \rangle)$$
(82)

The right hand side of (82) is the product of H and the dimensionless stress corresponding to the dipole energy. This dipolar stress will vary for the two extreme cases because the dot products $\langle \hat{\pmb{p}}_1 \cdot \hat{\pmb{r}} \rangle$ and $\langle \hat{\pmb{p}}_2 \cdot \hat{\pmb{r}} \rangle$ depend on placement of neighboring crystalline domains, which affects $\hat{\pmb{r}}$. In the parallel case $(\pmb{R} = R\hat{\pmb{e}}_3)$, an increase of field will yield $\langle \hat{\pmb{p}}_1 \cdot \hat{\pmb{r}} \rangle \rightarrow 1$, and $\langle \hat{\pmb{p}}_2 \cdot \hat{\pmb{r}} \rangle \rightarrow 1$. In contrast, as the field increases in the perpendicular case $(\pmb{R} = R\hat{\pmb{e}}_1)$, the dot products will approach towards $\langle \hat{\pmb{p}}_1 \cdot \hat{\pmb{r}} \rangle \rightarrow 0$, and $\langle \hat{\pmb{p}}_2 \cdot \hat{\pmb{r}} \rangle \rightarrow 0$. The assessments of $\langle \hat{\pmb{p}}_1 \cdot \hat{\pmb{r}} \rangle$ are performed by sampling a set of dipole moments from the von Mises distribution. The electric field dependence of these dot products causes the dipolar stress to be driven by the electric field, for which we choose a dimensionless parameter, $E^* = E/E_s$, implemented into (51) to obtain the orientation distribution parameter b_{Φ_p} used to calculate dipole moment angles.

To visually illustrate equilibrium, the two sides of (82), representing the elastic and dipolar stresses, are plotted versus λ in Fig. 11. The parameter H is set to 1 (one). The intersection between the elastic and the dipolar stress differences indicates the equilibrium stretch-state for the traction-free body. Fig. 11a plots the stress differences for the parallel case, and Fig. 11b for the perpendicular case. Initially in each figure, at $E^* = 0$ the dipole energy is identically zero and the elastic energy crosses the y-axis at $\lambda = 1$ signaling the undeformed state as expected. As E^* increases, the dipolar stress difference curve amplifies, shifting the equilibrium towards the left, meaning a contraction in the \hat{e}_3 direction (i.e., electrostriction response). However, while the perpendicular case in Fig. 11b depicts intersection over the full range of E^* shown, the parallel case in Fig. 11a becomes tangent to the dipole stress near $E^* = 7$. Consequently, beyond $\lambda = 7$ there is no solution to (82). This phenomenon can be physically interpreted as the field strength at which the dipolar stresses overcome the elastic stresses of the material, resulting in a phenomenon similar to the pull-in instability, as defined in Zhao and Wang (2014).

This type of mechanical failure has been studied for dielectric materials (i.e., pull-in instability), but it has not been studied for RFE polymers in the same manner (Plante and Dubowsky, 2007; Zhao and Suo, 2009; Dorfmann and Ogden, 2017; Zhao and Wang, 2014). Pull-in instability in dielectric elastomers is typically studied via the energy for an ideal linear dielectric material with a Neo-Hookean elastic model, as developed in Zhao and Wang (2014), in the form of

$$W_{LD} = C_{10} \left(\lambda^2 - 2\lambda^{-2} - 3 \right) + \frac{\lambda^2 D^2}{2\varepsilon}, \tag{83}$$

where $C_{10} = \frac{1}{2}NkT$, ε is the dielectric constant, and D is the electric displacement in the \hat{e}_3 direction. The nominal stress calculated by Zhao and Wang (2014) is

$$s_3 = C_{10} \left(\lambda - \lambda^{-2} \right) + \frac{\lambda D^2}{\varepsilon},\tag{84}$$

and D is related to E by the relation,

$$E = \frac{Y}{h} = \frac{\lambda^2 D^2}{\varepsilon},\tag{85}$$

in which Y is the voltage and h is the distance between two compliant electrodes attached to the dielectric elastomer. Substituting (85) into (84) and setting $s_3 = 0$ for traction free equilibrium yields

$$\sqrt{\frac{\varepsilon}{C_{10}}} \frac{Y}{h} = \sqrt{\left(\lambda - \lambda^4\right)}.$$
 (86)

Multiple similarities can be drawn between (86) and (82). Namely, the left- and right-hand sides of both equations represent stresses related to either the elastic or the dipolar energies, with a coefficient $H = \sqrt{\varepsilon/C_{10}}$ in (86) and $H = P_{sat}^2/(3C_1v_c\epsilon)$ in (82). In our model, ϵ represents the electric permittivity of the medium between the dipoles, whereas in the linear dielectric model, ϵ represents the average permittivity (or dielectric constant) of the entire material. Meanwhile, the differences between the two approaches are evident when considering the physical representations of the models. While the energies explored in our proposed model can be attributed to the interactions between domains and the amorphous phase's elastic response, the dielectric and elastic energy components in (83) are not based on any microstructure characteristics, and instead rely on phenomenological modeling.

The electrostrictive response of a material can be calculated by solving the nonlinear Eq. (82) for pairs of $[E, \lambda]$. The percent strain S_{33} (%) commonly reported in experimental results can be related to λ by

$$S_{33} = 100 * \ln \lambda,$$
 (87)

yielding pairs of $[E, S_{33}]$. These pairs, when plotted over a range of E, define electrostriction; hence, the relationship between E and S_{33} will be referred to as electrostriction in subsequent discussions.

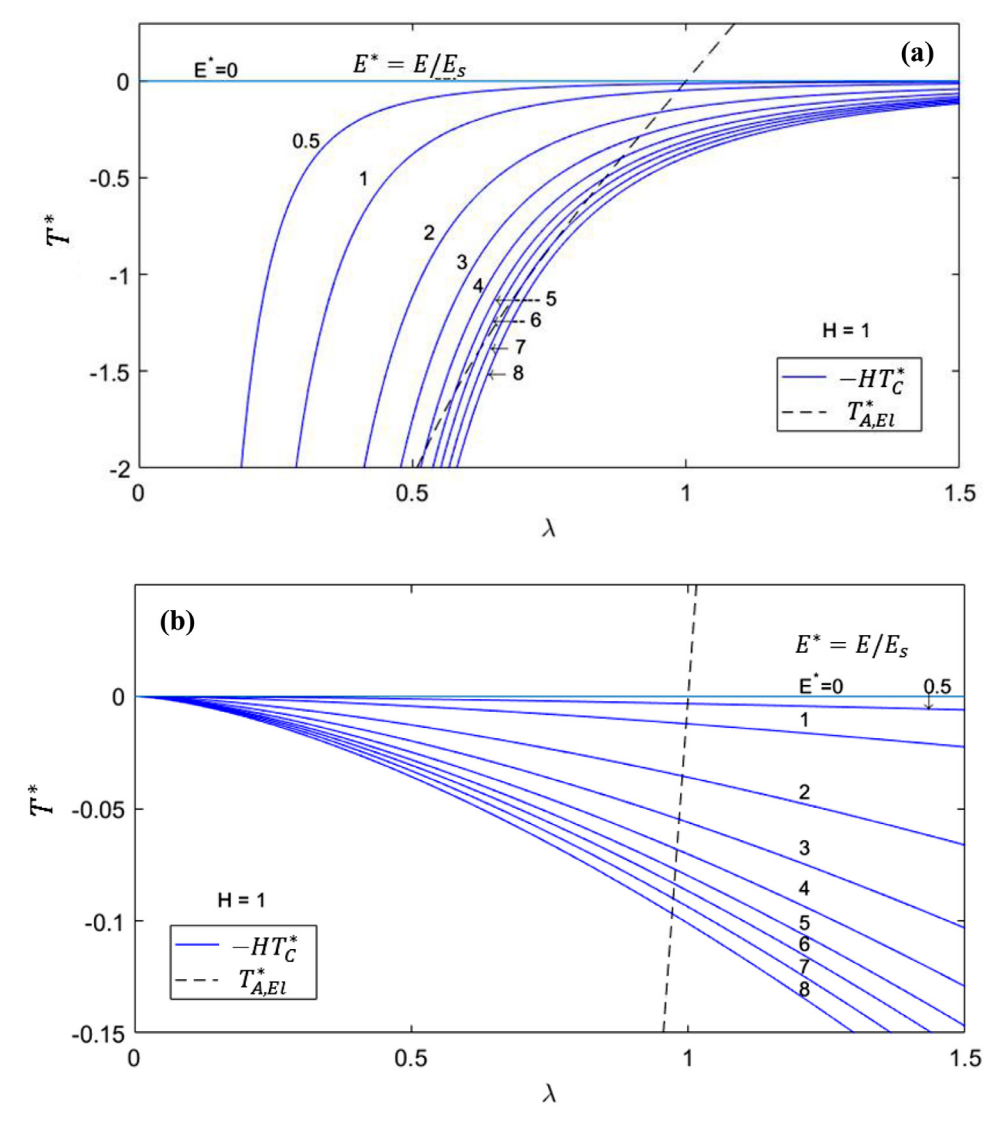


Fig. 11. The left- and right-hand sides of (82) are plotted versus λ for the extreme cases, (a) parallel single chain, and (b) perpendicular single chain. The blue line is the stress difference associated with the dipolar energy. The intersections of the curves indicate the equilibrium locations. (For interpretation of the references to colour in this figure legend, the reader is referred to the web version of this article.)

5.3. Derivation of the PDF-based network model

In this section, we consider averaging techniques for the *spatial* orientation aspect of the dipole-dipole interaction energy function, e.g. **r**. This is not to be confused with the von Mises probability density function applied to the distribution of *dipole moment vector* orientations. A probability distribution function will enable exploring the effect of intermediate orientations between the parallel and perpendicular cases on the electrostrictive response.

Consider a single (central) dipole residing in the RVE surrounded by a probability density of neighboring dipoles at some distance r from the central dipole and some azimuthal angle Φ_r . The total interaction energy of the system is the volume average scaled by the corresponding probability density, given by

$$\langle W_C \rangle = \frac{1}{A_f} \int_{-\pi}^{+\pi} f_{\Phi_r}(\Phi_r) W_d(\Phi_r) \sin \Phi_r d\Phi_r, \tag{88}$$

where $f_{\Phi_r}(\Phi_r)$ is a distribution function for the spatial orientations of dipoles. However, W_C must be calculated discretely to assess the dipole-dipole interactions under realist conditions; thus, an analytical solution is not obtainable to the continuous

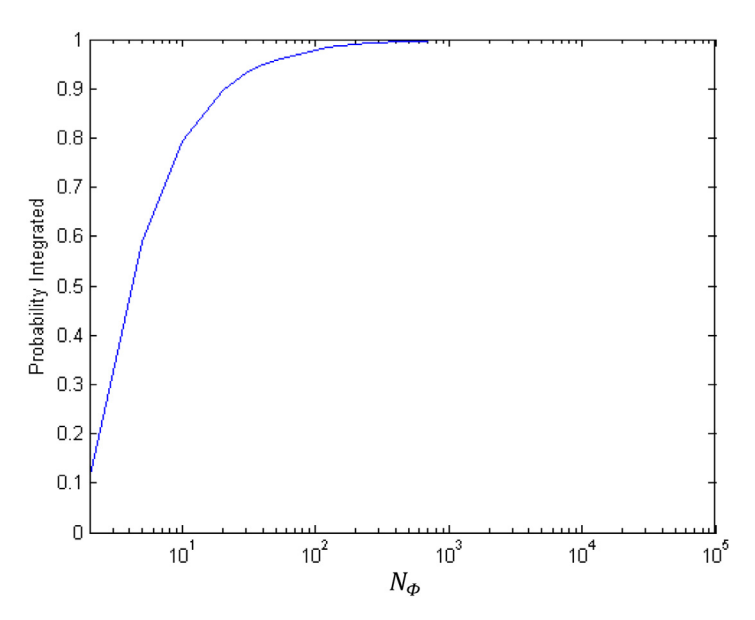


Fig. 12. The discretized distribution function in (89) is evaluated at $W_C(\Phi_{ri}) = 1$ for varying values of N_{Φ_r} .

integral in (88). As a result, the PDF-based average of W_C is calculated discretely below, in (89).

$$\langle \langle W_C \rangle \rangle = \frac{1}{A_f} \sum_{i}^{N_{\Phi_r}} f_{\Phi_r}(\Phi_{ri}) W_d(\Phi_{ri}) \Delta \Phi_r. \tag{89}$$

where the double bracket $\langle\langle \cdot \rangle\rangle$ denotes the discrete average. Given a small arc length, $\Delta \Phi_r$, discretization offers a viable option to solve the integral in (88). Furthermore, $\Delta \Phi_r$ is directly related to N_{Φ_r} by

$$\Delta\Phi_r = \frac{2\pi}{N_{\Phi_r}}.\tag{90}$$

A convergence study on the averaged energy in (89) evaluated at $W_C(\Phi_{ri}) = 1$ is plotted in Fig. 12, revealing that $N_{\Phi_r} = 500$ is sufficiently large to yield an approximation with less than 0.1% error compared to the integral in (88) with $W_C(\Phi_{ri}) = 1$.

To determine the spatial distribution function $f_{\Phi_r}(\Phi_r)$, we consider the location of any dipole, earlier defined as \mathbf{r}_{ij} , which lies on the surface ∂V of a sphere. Assuming axisymmetry, the spatial distribution can be defined as a 1D von Mises distribution on $\Phi_r \in [0, \pi]$,

$$f_{\Phi_r}(\Phi | \mu_{\Phi_r}, b_{\Phi_r}) = \frac{e^{b_{\Phi_r}\cos(\Phi_r - \mu_{\Phi_r})}}{2\pi I_0(b_{\Phi_r})},\tag{91}$$

where μ_{Φ_r} is the mean, and b_{Φ_r} is the concentration of the distribution of azimuthal angles Φ_r . As depicted in (82), the dipolar energy is not dependent on Θ , and consequently, the probability density is not affected by Θ , again a consequence of assuming isotropy in-plane. Moreover, the only adjustable parameters in this model is b_{Φ_r} because the mean is assumed collinear with the applied field direction $\hat{\boldsymbol{e}}_3$; hence $\mu_{\Phi_r} = 0$.

The averaged dipolar energy can be written by substituting (68) and (91) into (89), yielding

$$\left\langle \left\langle \bar{W}_{C} \right\rangle \right\rangle = \sum_{i=1}^{N_{\Phi_{r}}} \left[\frac{e^{b_{\Phi_{r}}\cos(\Phi_{r} - \mu_{\Phi_{r}})}}{2\pi I_{0}(b_{\Phi_{r}})} \right] \left[\frac{P_{sat}^{2} \left[\left\langle \hat{\boldsymbol{p}}_{1} \cdot \hat{\boldsymbol{p}}_{2} \right\rangle - 3\left\langle \hat{\boldsymbol{p}}_{1} \cdot \hat{\boldsymbol{r}} \right\rangle \left\langle \hat{\boldsymbol{p}}_{2} \cdot \hat{\boldsymbol{r}} \right\rangle \right]}{3N_{\Phi_{r}} v_{c} \epsilon \left(\lambda^{-1} \sin^{2} \Phi_{r} + \lambda^{2} \cos^{2} \Phi_{r} \right)^{3/2}} \right]. \tag{92}$$

The distribution parameter is defined as $b_{\Phi_r} \in [0, \infty)$. Due to its undefined maximum, b_{Φ_r} is difficult to relate to a physical structure. For performing a microstructure-based analysis, the model will be evaluated with respect to $\kappa \in [0, 1/3]$, which, given the von Mises distribution, has been used to discuss various physical structures in literature (Gasser et. al., 2006). It is evaluated as

$$\kappa = \frac{1}{4} \int_0^{\pi} f_{\Phi_r}(\Phi \mid \mu_{\Phi_r}, b_{\Phi_r}) \sin^3 \Phi_r d\Phi_r, \tag{93}$$

and as a result, (91) can be plotted as a function of κ . The significance of κ is that it is a more physically relatable term; $\kappa = 0$ implies a singular orientation with unit probability, while $\kappa = 1/3$ implies a uniform distribution. Since $\kappa \in [0, 1/3]$ is a clearly defined parameter, it will be used in the remaining calculations and analyses.

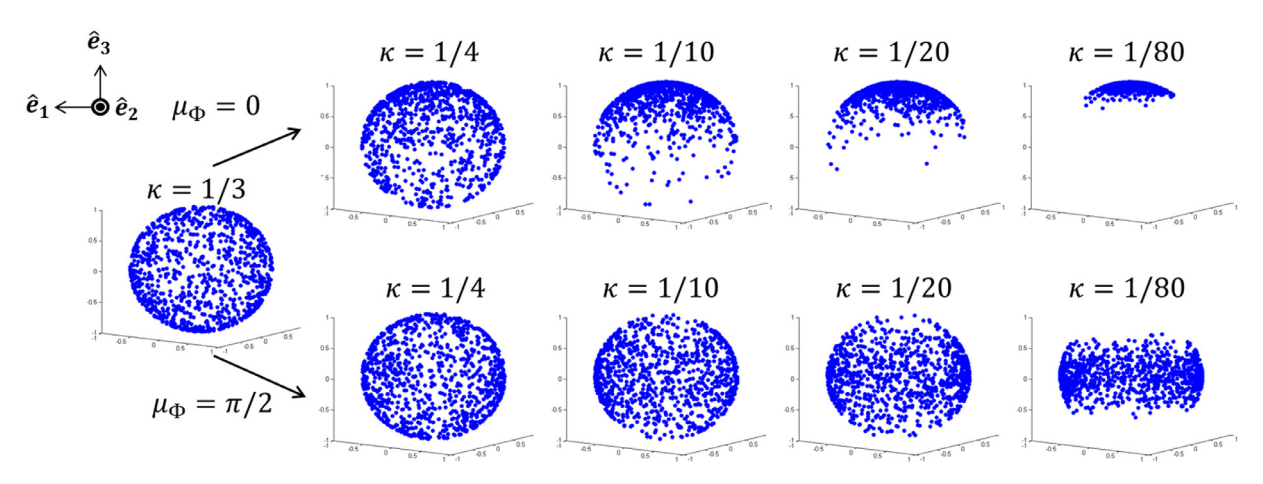


Fig. 13. The von Mises PDF is graphically represented by a scatter plot of randomly generated points based on the distribution evaluated at varying values of κ . The PDF is centered either at $\mu_{\Phi_r} = 0$ and $\mu_{\Phi_r} = \pi/2$ as shown, where these distributions move toward approximating the parallel and perpendicular discrete single chain models.

Various configurations of the distribution in (91) can be conceived by modifying μ_{Φ_r} and κ , as an alternative to the single chain network models. The distributions can be visualized by scatter plot of randomly generated points based on the distribution, as in Fig. 13. The examples shown in Fig. 13 are in the reference configuration, representing the spatial distribution of dipoles over an initially spherical, undeformed state of the RVE. Each point indicates a dipole that interacts with the central dipole. The spatial distribution is plotted for two cases, $\mu_{\Phi_r} = 0$ and $\mu_{\Phi_r} = \pi/2$ (representing nominally parallel and perpendicular single chain RVEs), at $\kappa = 1/3$, 1/4, 1/10, 1/20, 1/80. The distribution at $\kappa = 0.333$ is a uniform distribution, and thus it is the same for any μ_{Φ_r} . As κ is gradually decreased, the points begin coalescing towards their respective centers; eventually, as $\kappa \to 0$, all points will reside at a single location.

5.4. Analysis of the response of the PDF-based single chain network model

This subsection evaluates the total energy density substituted into (82) at varying electric field strengths to simulate the electromechanical response of the material. To study the effects of the distribution function introduced in Section 5.3, the averaged dipolar energy in (92) replaces the second term in (75), yielding

$$\langle \bar{W} \rangle = \frac{(1 - \nu_c)}{A_{el}} \sum_{i}^{N_{\Theta}} \sum_{j}^{N_{\Phi}} f_{sc} (\Phi_j, \Theta_i) W_{8ch} (I_1^A (\lambda, \Phi_j, \Theta_i), \lambda_m, C_1) sin \Phi \Delta \Theta \Delta \Phi
+ \left(\frac{P_{sat}^2 F(E)}{3N_{\Phi_r} \nu_c \epsilon} \right) \sum_{i=1}^{N_{\Phi_r}} \left[\frac{e^{b_{\Phi_r} \cos(\Phi_r - \mu_{\Phi_r})}}{2\pi I_0(b_{\Phi_r})} \right] \left[\frac{1}{(\lambda^{-1} \sin^2 \Phi_{ri} + \lambda^2 \cos^2 \Phi_{ri})^{3/2}} \right].$$
(94)

The stress differences based on this energy can be calculated in the same manner as in (81) and (82) by non-dimensionalizing via $H = P_{sat}^2/(C_1\epsilon)$.

To highlight the dependence of $\langle \bar{W} \rangle$ on E, we use $F(E) = \langle \hat{\pmb{p}}_1 \cdot \hat{\pmb{p}}_2 \rangle - 3 \langle \hat{\pmb{p}}_1 \cdot \hat{\pmb{r}} \rangle \langle \hat{\pmb{p}}_2 \cdot \hat{\pmb{r}} \rangle$, which combines the terms indirectly related to E via the orientation distribution function in Section 4.2. The value of N_{Φ} is set to 50, determined from the convergence study in Section 5.3. The variable λ is solved for by substituting (94) into (67) and solving for pairs of $[E, \lambda_3]$, which are transformed via (87) into $[E, S_{33}]$. Recall that this relationship between E and E0 was defined earlier as electrostriction. Based on fitting of the eight-chain hyperelastic model in (32) to experimental data performed later in this paper, we chose $k_m = 2.5$ for the following model calculations. Consequently, the model will be capable of plotting electrostriction with only a few adjustable parameters, k_{Φ_T} , and k_T .

The electrostriction model can be analyzed by varying the two adjustable parameters in the context of the earlier defined parallel and perpendicular cases. We consider two cases for μ_{Φ_r} that approximate the parallel and perpendicular models: $\mu_{\Phi_r} = 0$ and $\mu_{\Phi_r} = \pi/2$, respectively. For these two cases, the model calculates the electrostrictive response of (94) at varying dispersion factors, κ , as plotted in Fig. 14. Note that the electrostriction is plotted in terms of a normalized strain, $S_{33}^* = S_{33}/S_{max}$, where S_{max} is the maximum obtained strain in all of the electrostriction calculations, and a normalized electric field $E^* = E/E_{sat}$. As $\kappa \to 1/3$, the distribution functions for both cases, $\mu_{\Phi_r} = 0$ and $\mu_{\Phi_r} = \pi/2$, are identically uniform, and thus, the electrostrictive responses of both cases converge at a value as shown in Fig. 14a, indicating internal consistency of the model. In contrast, as $\kappa \to 0$, the distributions rapidly diverge, and their electrostrictive responses diverge toward separate asymptotes at Fig. 14 point c and Fig. 14 point e. Specifically, as $\kappa \to 0$ for $\mu_{\Phi_r} = 0$, the electrostriction significantly increases as the distribution function approaches a singular point, as shown in Fig. 14 point c. However, as $\kappa \to 0$

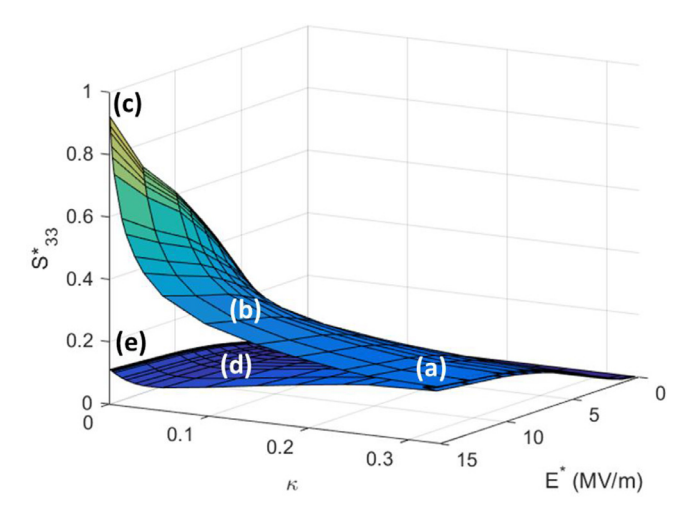


Fig. 14. Comparison of the two extreme cases with PDFs in prediction of electrostriction. As $\kappa \to 1/3$, both PDF-based responses converge toward the discrete network responses, which is why the discrete network models are placed at the low end of the κ range. Due to theoretical material failure, electrostriction could not be determined at field strengths above $E^* = 15$ for $\mu_{\Phi_r} = 0$ as $\kappa \to 0$; as a result, saturation is not observed at (c).

Table 1Terpolymers are listed with chemical composition and processing details. The chemical compositions may differ from the literature because they have been normalized here to add up to 100%.

Polymer	Percent composition Additional processing	
P(VDF-TrFE-CTFE)	61.8/30.4/7.8%	Annealed at 120 °C for 9 h
P(VDF-TrFE-CTFE) (Xu et al., 2001)	59.1/31.8/9.1%	Annealed at 100–120 °C for 6 h
P(VDF-TrFE-CFE) (Cheng et al., 200X)	59.6/36.5/3.8%	Annealed at 110 °C for an unspecified period

for $\mu_{\Phi_r} = \pi/2$, the electrostriction observes a small decrease, shown in Fig. 14 point e. These results imply that the forces generated by dipoles whose relative positions are parallel to the field-direction dominate the electrostriction response of a material, and to maximize the electrostrictive response of a material, the target microstructure should contain crystalline domains that are aligned parallel to the direction of the field (often the direction of the thickness). However, it should be noted that the model failed to compute pairs of $[E, S_{33}]$ for $\mu_{\Phi_r} = 0$ below $\kappa \cong 0.0005$, shown in Fig. 14 point c, due to the material failure phenomenon discussed in Section 5.2. Thus, spatially aligning domains to a very high order of $\kappa < 0.001$ may be counterproductive as it may trigger material failure at high field strengths. As a result, perfectly (spatially) aligned domains may not be desired, especially at field strengths above $E^* = 15$.

An anomaly in the energy functions is revealed near Fig. 14 point d, where the electrostriction for $\mu_{\Phi_r} = \pi/2$ observes a dip near $\kappa \cong 0.05$. This behavior reflects the phenomenon introduced earlier in Section 5.2, where the possibility of a state of orientation between $0 < \Phi_r < \pi/2$ yielding zero interaction energy was mentioned. Furthermore, due to the relatively weak energy at $\Phi_r = \pi/2$, the zero-energy orientation affects the averaging of the energy more significantly for $\mu_{\Phi_r} = \pi/2$, thus causing the drop in electrostriction at Fig. 14 point d. Considering this phenomenon, alignments in the diagonals may not be ideal for achieving a high electrostrictive response.

5.5. Comparisons of network model responses to experimental data

This subsection studies the effectiveness of the model in terms of predicting the behavior of EAPs, as well as its ability to address variability of relative spatial locations of crystalline domains. The electrostriction model will be compared to multiple data sets by first determining material constants from experiments, then fitting the PDF-based network model via adjustment of κ .

Three materials have been chosen in this study. One of the materials was fabricated and tested by us, while the remaining two material data sets were borrowed from literature. All three materials are P(VDF)-based terpolymers; their processing methods are listed along with their chemical compositions in Table 1.

All three terpolymers were synthesized by bulk polymerization. The material fabricated for this study is polyvinylidene-trifluoroethylene-chlorotrifluoroethylene, also known as P(VDF-TrFE-CTFE) 61.8/30.4/7.8%.

The polarization model in Capsal et al. (2012), which is based on (50), was used to determine the saturation polarization of the material by least squares fitting the polarization model to experimental data from our laboratory and borrowed from literature. Fig. 15 shows the fitted models to each set of measured data. Results are tabulated in Table 2 and used to determine electrostriction in Eqs. (67) and (94).

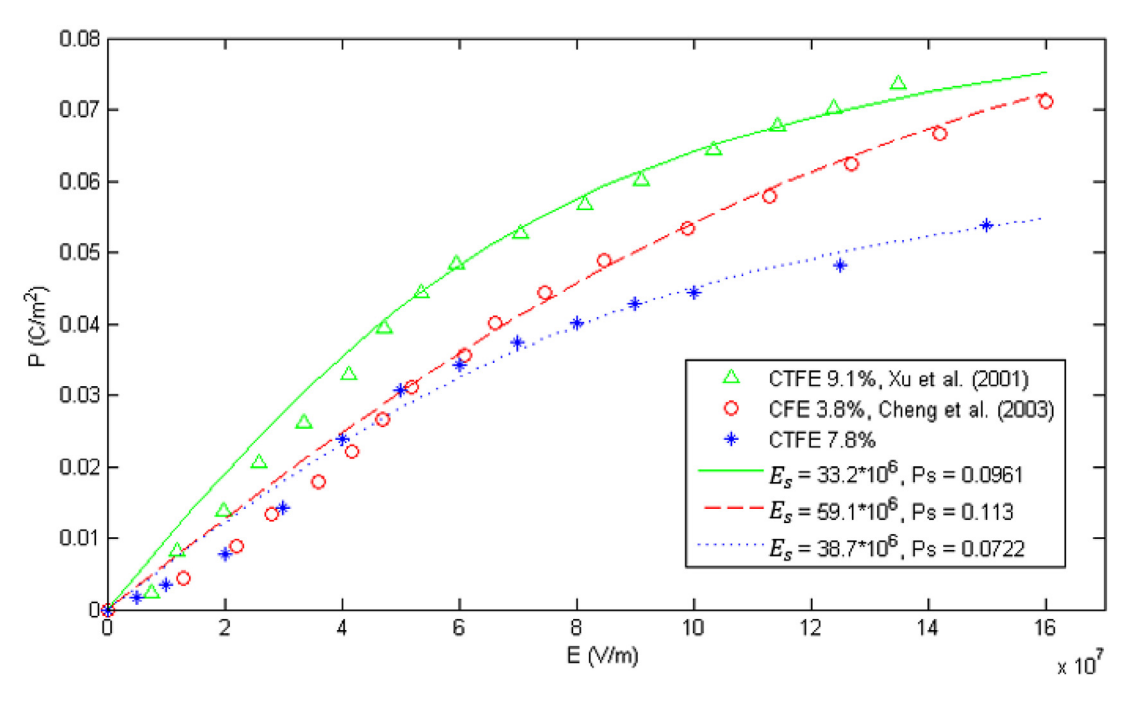


Fig. 15. The single-phase polarization model is fitted to the polarization responses of three data sets. The fitted parameters P_s and E_s (in legend) are also listed in Table 2.

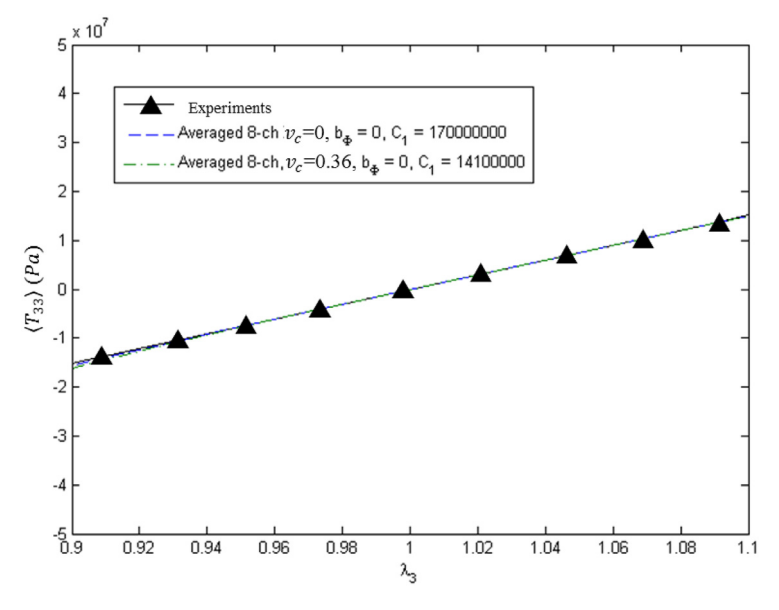


Fig. 16. Tensile test data for the CTFE 7.8% terpolymer, and two best-fit models: modified 8-chain hyperelastic model $W_{8ch}(l_1^A)$ with crystallinity $\nu_c = 0$ and $\nu_c = 0.36$.

The elastic properties of P(VDF-TrFE-CTFE) 7.8% are determined by fitting the modified eight chain hyperelastic model $W_{8ch}(I_1^A)$ to experimental tensile data conducted in our laboratory (not shown). The energy is fitted for $v_c = 0.36$ (actual crystallinity) and also $v_c = 0$ to study the effects of crystallinity. The energy with zero crystallinity will provide us a measure of an average C_1 , while the corrected energy apportioned to only the amorphous phase will provide us a C_1 value for only the amorphous phase. As shown in Fig. 16, the best fit for the average and amorphous C_1 constants are 170 MPa and 14.1 MPa, respectively. The amorphous phase's C_1 is more than an order of magnitude lower than the average, which is expected, as the rigidity of the crystallites will significantly increase the average elastic response of the material. Note that the models are fitted to experiments within a small range of λ , because electrostriction often does not exceed 10% strain.

Table 2 Parameters used for the simulations in Fig. 15.

	ν _c (%)	C ₁ (MPa)	λ_m	Y(GPa)	ϵ_r	$P_s \left(\frac{C}{m^2}\right)$	E _s (MV/m)
P(VDF-TrFE-CTFE) 61.8/31.4/7.8%	36	14.1	2.5	-	9.4	0.0722	38.7
P(VDF-TrFE-CFE) 59.6/36.5/3.8%	43	-	-	1.1	3.0	0.113	59.1
P(VDF-TrFE-CTFE) 59.1/31.8/9.1%	56	-	-	0.4	4.6	0.0961	33.2

For the other terpolymers, the reported Young's modulus is used and as a result, we employ a simple Neo-Hookean model to model the hyperelastic response of the material. Results are tabulated in Table 2 and used to predict electrostriction in Eqs. (67) and (94).

In addition to the saturation polarization, the permittivity of the amorphous phase ε_a is also required for calculating the dipole-dipole interaction energy. Thus, we utilize the biphasic model derived by Capsal et al. (2012), defined in (95). This model is fitted to each experimental data (both from our laboratory and borrowed from other studies) to obtain average values of the bulk permittivity $\varepsilon_{r, total}$. The biphasic model assumes that the crystalline phase dominates the material's polarization response at low field strengths of about 0–150 MV/m, and eventually the amorphous phase begins to dominate the material's response, behaving similar to a linear dielectric. Thus, we make the assumption that the amorphous phase has a constant permittivity of ε_a , to reduce the number of unknown variables.

$$\varepsilon_{r,total} = \frac{1}{\varepsilon_0} 3E_s(\varepsilon_c - \varepsilon_0) \left[-\frac{1}{\sin h^2(\frac{E}{E_s})} + \frac{E_s^2}{E^2} \right] + \varepsilon_a$$
 (95)

All literature data is analyzed by Web Plot Digitizer, which is an online tool that aids in extracting data points on an image. The images are analyzed by a step size of 1 pixel. The relative electric permittivity of a dielectric material is defined as

$$\varepsilon_r = \frac{1}{\varepsilon_0} \frac{dP}{dE} + 1,\tag{96}$$

in which ε_r is the relative electric permittivity, P is the polarization, and E is the electric field. We must determine the permittivity by approximating the derivative of the polarization with respect to the electric field, which can be determine from a set of data as

$$\frac{dP}{dE}\Big|_{i} \approx \frac{P(i+1) - P(i+1)}{E(i+1) - E(i-1)} \text{ (for } i = 1, 2, \dots n_{P}).$$
(97)

Once we obtain a set of permittivity data, we fit the model to the data by a least squares method to determine ϵ_r . Given known variance in the polarization data for P(VDF-TrFE-CTFE) 7.8%, we fit the model to one standard deviation below, one standard deviation above, and exactly at the average measured values. As a result, we obtain a range of permittivity for the amorphous phase for this material, from 4.0 to 14, with an average of 9.4. Variance in the other materials are studied by exploring the effects of adding weights to the least squares fitting method to prioritize the polarization responses at higher field strengths, which will better reflect the amorphous phase's permittivity. Due to the complexity of extracting the exact value of ϵ_r from experiments, we focused on using approximate (averaged) values of ϵ_r instead of analyzing a spectrum of ϵ_r per material (such an analysis is beyond the scope of this paper). The approximate results are listed in Table 2. The relatively low permittivities for the amorphous phase are consistent with the theory that the amorphous phase should have a low dielectric response compared to the crystalline phase.

The parameters listed in Table 2 are used in the electrostriction model for each material at varying values of κ at $\mu_{\Phi_r}=0$ and $\mu_{\Phi_r}=\pi/2$. Fig. 17 shows the model evaluated at $0.025 \le \kappa \le 0.333$ for $\mu_{\Phi_r}=0$ and at $0.05 \le \kappa \le 0.333$ for $\mu_{\Phi_r}=\pi/2$ compared to data for P(VDF-TrFE-CTFE) 7.8%. The best-fit curve to experiments (by least square errors) is signaled by a dashed line, with the fitted values $\mu_{\Phi_r}=0$ and $\kappa=0.111$. A distribution of $f_{\Phi_r}(\Phi_r;\mu_{\Phi_r}=0,\kappa=0.111)$ leans towards a narrow distribution of neighboring RVE locations around the $\Phi_r=0$ (parallel) position. Furthermore, the fitted distribution may be interpreted as spatial distributions of crystalline domains, and consequently, the distribution represents an implied microstructure characteristic. The implied microstructure the fitted model for CTFE 7.8% RFE polymer contains crystalline domains with relative locations that are to varying degrees parallel with respect to the field, as depicted in Fig. 13.

A similar fitting procedure is performed for the CTFE 9.1% RFE polymer, and the model is plotted over the same range of distributions in Fig. 19. For this material, the best-fit distribution is $f_{\Phi_r}(\Phi_r; \mu_{\Phi_r} = 0, \kappa = 0.145)$, indicating a very similar distribution to the best-fit model for the CTFE 7.8% polymer. Similarly, the best-fit model implies that neighboring crystalline domains would be at varying degrees of alignment to the applied-field direction, with most concentrated at the parallel orientation.

It is important to note that the comparisons in Figs. 17 and 19 reveal a best-fit model with a distribution center of $\mu_{\Phi_r}=0$ and a moderate degree of spatial alignment. Despite their moderately narrow distributions, the best-fit models for the CTFE RFE polymers still show considerable probabilities of spatial arrangements of neighboring crystallites far beyond $\Phi_r=0$ (see Fig. 13). Conversely, the model comparisons for P(VDF-TrFE-CFE) 9.1% result in a very narrow distribution of

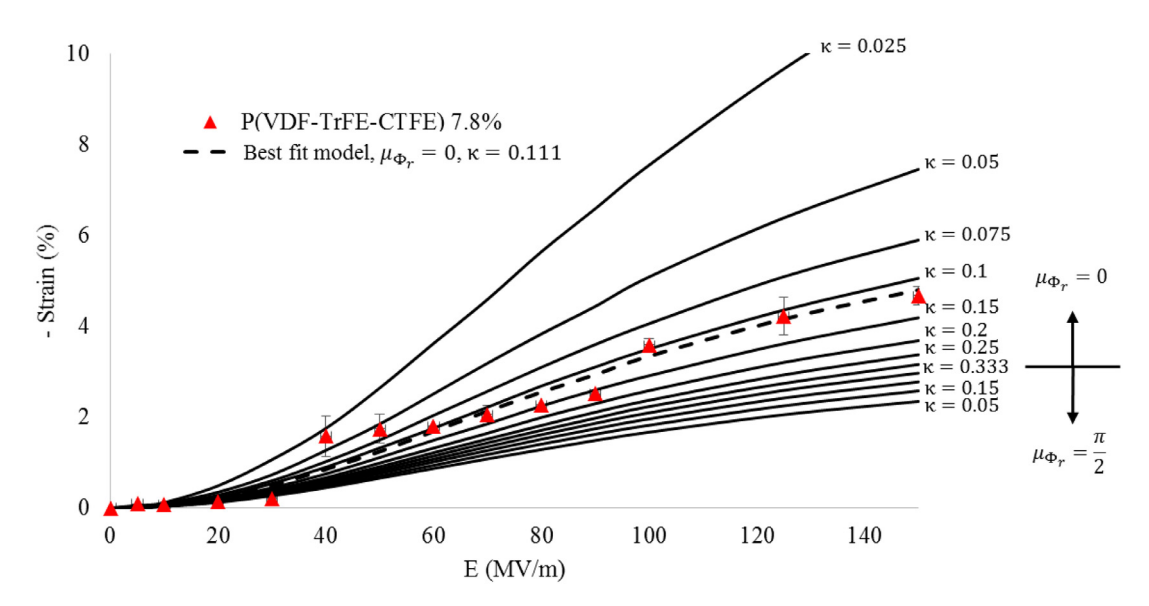


Fig. 17. Comparison of the electrostriction model evaluated at varying distribution parameters with experiments for P(VDF-TrFE-CTFE) 7.8%.

 $f_{\Phi_r}(\Phi_r; \mu_{\Phi_r} = 0, \kappa = 0.034)$, which is between the visual depictions of $\kappa = 1/80$ and $\kappa = 1/20$ in Fig. 13. Such a distribution implies very little variation beyond the parallel arrangement.

Beyond fitting the electrostriction model to experiments, the model may be used predictively to determine microstructures required for desired properties. It is apparent from the model-experiment comparisons (as well as preliminary comparisons of nondimensionalized energies) that spatial distributions centered parallel to the field with very narrow widths generate the largest electrostrictive responses. Consequently, we would prefer to fabricate materials with similar microstructural arrangements. For example, Fig. 17 implies that, if the predicted microstructure for the tested P(VDF-TrFE-CTFE) 7.8% terpolymer is correct, it is possible to increase the material's electrostrictive response by more than a factor of 2 if we reduce the distribution width to $\kappa = 0.025$ through material processing techniques during fabrication, which would theoretically yield greater than 10% electrostrictive strain at 150 MV/m. Using this method, the model may assist materials scientists to assess the performance envelope of a given set of fabrication methods, or achieve target materials properties through tailored processing. However, it is important to note that due to a lack of availability of experimental data on spatial arrangements of crystallites within RFE polymer microstructures, it is currently not feasible to validate the model's predictive capabilities. Furthermore, a validation procedure is necessary before the model can be used for targeting desired material properties. Nonetheless, the model's significance remains from its ability to address the microstructural characteristics that would be necessary to predict structure-property relationships.

Although the model fits the experimental data well, especially at high field strengths (above 100 MV/m), some characteristics of the curves are not captured entirely at lower field strengths. For example, there is a relatively high error in fitting the model to CTFE 7.8% at approximately 40 MV/m in Fig. 17. This is due to a spike in electrostriction observed in experiments; it is hypothesized that these spikes may result from two separate crystalline phases. Based on in situ X-ray diffraction (XRD) data on CTFE 7.8% terpolymer, β -phase has a coercive field around 40–50 MV/m, which may explain the electrostrictive spike. Additionally, a similar spike is observed for CTFE 9.1% at 50 MV/m in Fig. 18. The relatively low initial electrostrictive response in the experimental data for CTFE 7.8% (Fig. 17) may also be due to the resolution of the experimental measurements, which could amplify the spike at 40 MV/m. These spikes are not as clearly observed in the other data sets. Additionally, predicting low-field responses may be improved by adding the effects of dipole-induced fields. However, including dipole-induced fields in a local field calculation would create new computational challenges beyond the scope of this study.

6. Concluding remarks

The spatial and orientation distributions of polarizable crystalline regions within RFE polymers, which may be controlled through composition and processing, affect the electromechanical coupling and consequently are important quantities to any modeling attempt. The spatial organization of the crystalline regions formed in these RFE polymers during processing varies, requiring the development of a model capable of capturing what is known about their morphology. The present model addresses such information in the morphology by applying distributions of orientations and spatial arrangements into the mechanics of a semicrystalline (biphasic) RVE. The driving mechanism of the RVE's deformation is the domain-domain interactions between the RVE crystalline domain and a neighboring RVE's crystalline domain. The dipole-dipole interaction energy of the two crystallites competes with the elastic energy of the chain, which results in a change in the equilibrium

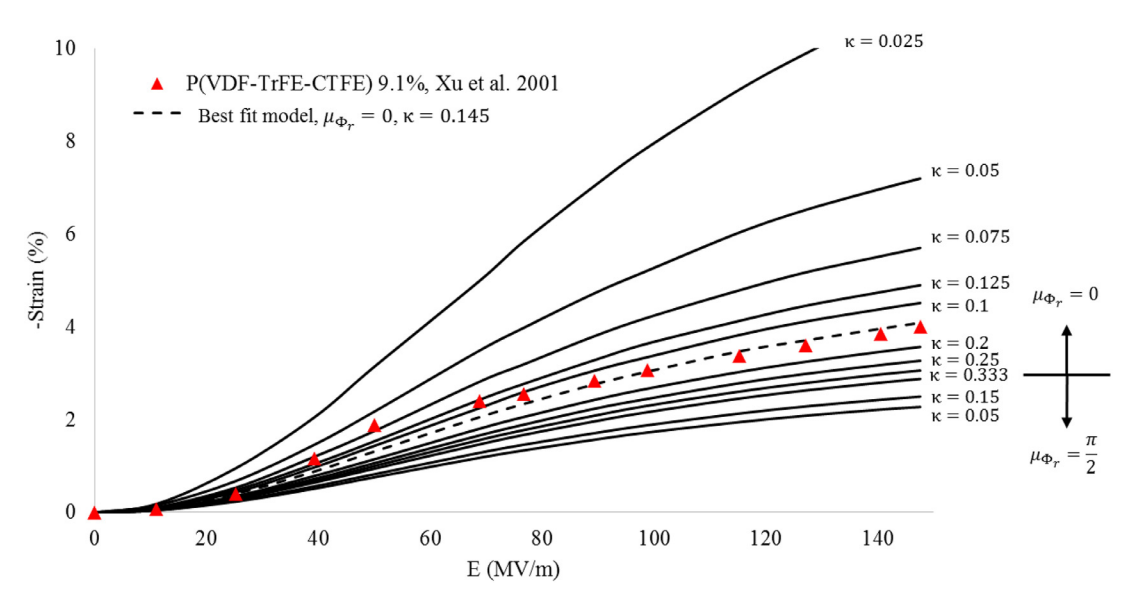


Fig. 18. Comparison of the electrostriction model evaluated at $0 < \kappa < 1/3$ for $\mu_{\Phi} = 0$ and $0.05 < \kappa < 0.\overline{3}$ for $\mu_{\Phi} = \pi/2$ with experiments for P(VDF-TrFE-CTFE) 9.1%.

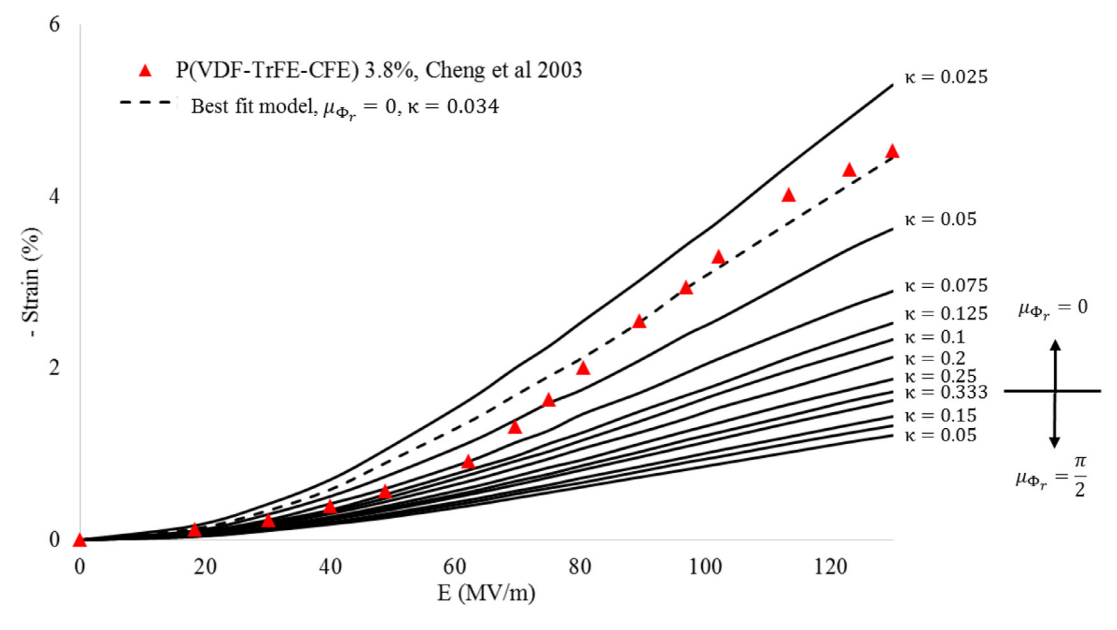


Fig. 19. Comparison of the electrostriction model evaluated at varying distribution parameters with experiments for P(VDF-TrFE-CFE) 3.8%.

of the system (i.e., strain). Since the domain-domain interactions are dependent on both the orientations of the crystalline domains and their relative spatial placements, von Mises distributions were applied to each to evaluate the dependence of the response on those distributions.

The model is effective at relatively high field strengths (i.e., near saturation), but with one date set, there are nonlinearities that are not fully captured at low-field strengths (i.e., typically within 0–50 MV/m). The low-field errors in this data set are attributed to the existence of multiple crystalline phases in the microstructure, where weaker phases align before shifting into larger and more polar phases. To account for the multiple crystalline phases, additional orientation distributions may be added into the calculation of the domain-domain interaction, and each distribution may be triggered at different field strengths to represent phase shifts. In addition, boundaries between domains may be described smoothly by distribution functions of their own, and dipole-induced fields may be included in local field derivations that would drive the polarization orientations of domains.

The modeling results also highlight that the relative positions of crystalline domains parallel to the external field have a greater influence on the electrostrictive response over positions perpendicular to the external field direction. An under-

standing of which relative position are more dominant in electrostriction may aid in the development of better performing electrostrictive materials. The model may also be used to predict pull-in instabilities, which are strongly affected by the spatial distributions, that cause material failure. Accounting for variance in spatial locations within a biphasic network models is a significant improvement over previous modeling techniques, which have ignored these distributions in a semicrystalline framework.

The model framework allows for extension to higher fidelity with respect to microstructure. The model may be studied with different distribution centers in directions other than the discrete principle axes, such as multiple orientations used in 3-, 4- and 8-chain network models of hyperelasticity. An additional distribution may be added in the R-direction to study the effects of variance in distance between dipole centers. Finally, the present modeling framework may offer versatility in predicting electromagnetic field-dependent response of other dipole-based material groups, such as Magneto-Active Elastomers (MAEs) (Bustamante, 2010; von Lockette and Sheridan, 2013).

Acknowledgments

We gratefully acknowledge the support of the National Science Foundation EFRI grant number 1240459 and the Air Force Office of Scientific Research. Any opinions, findings, and conclusions or recommendations expressed in this material are those of the author(s) and do not necessarily reflect the views of the National Science Foundation.

Supplementary materials

Supplementary material associated with this article can be found, in the online version, at doi:10.1016/j.jmps.2018.09.024.

References

Ang, C., Yu, Z., 2005. "Dielectric relaxor" behavior of electroactive fluorinated polymers.". Appl. Phys. Lett. 86 (26), 262903.

Arruda, E.M., Boyce, M.C., 1993. A three-dimensional model for the large stretch behavior of rubber elastic materials. J. Mech. Phys. Solids 41 (2), 389–412. Ask, A., Menzel, A., Ristinmaa, M., 2015. Modelling of viscoelastic dielectric elastomers with deformation dependent electric properties. Procedia lutam 12, 134–144.

Bao, H.M., Song, J.F., Zhang, J., Shen, Q.D., Yang, C.Z. &, Zhang, Q.M., 2007. Phase transitions and ferroelectric relaxor behavior in P(VDF-TrFE-CFE) terpolymers. Macromolecules 40, 2371–2379.

Bar-Cohen, Y., 2002. Electroactive polymers: current capabilities and challenges. Smart Structures and Materials 2002: Electroactive Polymer Actuators and Devices (EAPAD), 4695. International Society for Optics and Photonics.

Bauer, F., et al., 2002. Ferroelectric Copolymers and Terpolymers for Electrostrictors: Synthesis and Properties. Electrets, 2002. ISE 11. Proceedings. 11th International Symposium on. IEEE.

Bustamante, R., 2010. Transversely isotropic nonlinear magneto-active elastomers. Acta Mech. 210 (3-4), 183-214.

Capsal, J.-F., et al., 2012. Evaluation of macroscopic polarization and actuation abilities of electrostrictive dipolar polymers using the microscopic Debye/Langevin formalism. J. Phys. D Appl. Phys. 45 (20), 205401.

Castañeda, Pte., Siboni, M.H., 2012. A finite-strain constitutive theory for electro-active polymer composites via homogenization. Int. J. Non Linear Mech. 47 (2), 293–306.

Cho, Y., et al., 2016. Enhanced Ferroelectric Property of P (VDF-TrFE-CTFE) Film Using Room-Temperature Crystallization for High-Performance Ferroelectric Device Applications. Adv. Electron. Mater. 2 (10), 1600225.

Chu, B., et al., 2006. Relaxor ferroelectric poly(Vinylidene Fluoride-TrifluoroethyleneChlorofluoroethylene) terpolymer for high energy density storage capacitors. IEEE Trans. Dielectr. Electr. Insul. 13 (5), 1162–1169.

Cohen, N., 2014. Multiscale analysis of the electromechanical coupling in dielectric elastomers. Eur. J. Mech.A/Solids 48, 48-59.

Cohen, N., Dayal, K., 2016. Electroelasticity of polymer networks. J. Mech. Phys. Solids 92, 105-126.

Cohen, N., deBotton, G., 2015. The electromechanical response of polymer networks with long-chain molecules. Math. Mech. Solids 20 (6), 721-728.

Dang, Z., Lin, Y., Nan, C., 2003. Novel ferroelectric polymer composites with high dielectric constants. Adv. Mater. 15 (19), 1625–1629.

Dorfmann, L., Ogden, R.W., 2017. Nonlinear electroelasticity: material properties, continuum theory and applications. Proc. R. Soc. A. 473 No. 2204. The Royal Society.

Duan, C-g., et al., 2004. Simulations of ferroelectric polymer film polarization: The role of dipole interactions. Phys. Rev. B 69 (23), 235106.

Eringen, Aal., 1963. On the foundations of electroelastostatics. Int. J. Eng. Sci. 1 (1), 127–153.

Flory, P.J., Rehner, J., 1943. Statistical theory of chain configuration and physical properties of high polymers. Annals of the New York Academy of Sciences 44 (1), 419–429.

Gasser, Tan., Ogden, R.W., Holzapfel, G.A., 2006. Hyperelastic modelling of arterial layers with distributed collagen fibre orientations. J. R. Soc. Interface 6, 15–35.

Guan, F., et al., 2010. Effects of polymorphism and crystallite size on dipole reorientation in poly (vinylidene fluoride) and its random copolymers. Macromolecules 43 (16), 6739–6748.

Hong, W., 2011. Modeling viscoelastic dielectrics. J. Mech. Phys. Solids 59 (3), 637–650.

Jiménez, S.M.A., McMeeking, R.M., 2013. Deformation dependent dielectric permittivity and its effect on actuator performance and stability. Int. J. Non Linear Mech. 57, 183–191.

Klein, R.J., et al., 2005. Influence of composition on relaxor ferroelectric and electromechanical properties of poly (vinylidene fluoride-trifluoroethylene-chlorofluoroethylene). J. Appl. Phys. 97 (9), 094105.

Lallart, M., et al., 2016. Modeling of hysteretic behavior in ferroelectric polymers. J. Polym. Sci. Part B Polym. Phys. 54 (4), 499-508.

Lu, Y., et al., 2006. Microstructures and dielectric Properties of the ferroelectric fluoropolymers synthesized via reductive dechlorination of poly (vinylidene fluoride-co-chlorotrifluoroethylene) s. Macromolecules 39 (20), 6962–6968.

Lu, Y., et al., 2008. Structural dependence of phase transition and dielectric relaxation in ferroelectric poly (vinylidene fluoride – chlorotrifluoroethylene – trifluoroethylene) s. J. Phys. Chem. B 112 (34), 10411–10416.

Miehe, C., 1998. A constitutive frame of elastoplasticity at large strains based on the notion of a plastic metric. Int. J. Solids Struct. 35 (30), 3859-3897.

Miehe, C., Zäh, D., Rosato, D., 2012. Variational-based modeling of micro-electro-elasticity with electric field-driven and stress-driven domain evolutions. Int. J. Numer. Methods Eng. 91 (2), 115–141.

Mooney, M., 1940. A theory of large elastic deformation. J. Appl. Phys. 11 (9), 582–592.

Nalwa, H.S., 1995. Ferroelectric polymers: Chemistry: Physics, and applications. CRC Press.

Nateghi, A., et al., 2018. An affine microsphere approach to modeling strain-induced crystallization in rubbery polymers. Continuum Mech. Thermodyn. 1–23.

Ogden, R.W., 1997. Non-linear elastic deformations. Cour. Corporation.

Plante, J.S., Dubowsky, S., 2007. On the properties of dielectric elastomer actuators and their design implications. Smart Mater. Struct. 16 (2), S227.

Rivlin, R., 1948. Large elastic deformations of isotropic materials. IV. further developments of the general theory. Philos. Trans. R. Soc. Lond. A 241, 379–397. Richards, A.W., Odegard, G.M., 2010. Constitutive modeling of electrostrictive polymers using a hyperelasticity-based approach. J. Appl. Mech. 77 (1), 014502. Sencadas, V., Gregorio, R., Lanceros-Mendez, S., 2009. Alpha to beta phase transformation and microstructural changes of PVDF films induced by uniaxial stretch. J. Macromol. Sci. B 48, 514–525.

Silva, M.P., et al., 2010. α -and γ -PVDF: Crystallization kinetics, microstructural variations and thermal behaviour. Mater. Chem. Phys. 122 (1), 87–92.

Skatulla, S., Sansour, C., Arockiarajan, A., 2012. A multiplicative approach for nonlinear electro-elasticity. Comput. Meth. Appl. Mech. Eng. 245, 243–255. Smith, O.L., et al., 2014. Enhanced permittivity and energy density in neat poly (vinylidene fluoride-trifluoroethylene-chlorotrifluoroethylene) terpolymer

films through control of morphology. ACS Appl. Mater. Interfaces 6 (12), 9584–9589. Toupin, R.A., 1956. The elastic dielectric. J. Ration. Mech. Anal. 5 (6), 849–915.

Treloar, L.R.G., 1943. The elasticity of a network of long-chain molecules-II. Trans. Faraday Soc. 39, 241-246.

Treloar, L.R.G., 1944. Stress-strain data for vulcanised rubber under various types of deformation. Trans. Faraday Soc. 40, 59–70.

Truesdell, C., Toupin, R., 1960. The Classical Field Theories. In: Principles of Classical Mechanics and Field Theory/Prinzipien der Klassischen Mechanik und Feldtheorie. Springer, Berlin Heidelberg, pp. 226–858.

von Lockette, P., Sheridan, R., 2013. Folding actuation and locomotion of novel magneto-active elastomer (MAE) composites. ASME Paper No. SMA-SIS2013-3222.

Wang, M.C., Guth, E., 1952. Statistical theory of networks of non-Gaussian flexible chains, I Chem. Phys. 20 (7), 1144-1157.

Wu, P.D., Van Der Giessen, Erik, 1993. On improved network models for rubber elasticity and their applications to orientation hardening in glassy polymers. J. Mech. Phys. Solids 41 (3), 427–456.

Xu, H., et al., 2001. Ferroelectric and electromechanical properties of poly (vinylidenefluoride-trifluoroethylene-chlorotrifluoroethylene) terpolymer. Appl. Phys. Lett. 78 (16), 2360-2362.

Yang, L., et al., 2013. Novel polymer ferroelectric behavior via crystal isomorphism and the nanoconfinement effect. Polymer 54 (7), 1709-1728.

Zäh, D., Miehe, C., 2015. Multiplicative electro-elasticity of electroactive polymers accounting for micromechanically-based network models. Comput. Meth. Appl. Mech. Eng. 286, 394–421.

Zäh, D., Miehe, C., 2013. Computational homogenization in dissipative electro-mechanics of functional materials. Comput. Meth. Appl. Mech. Eng. 267, 487–510.

Zhang, Q.M., Bharti, V., Zhao, X., 1998. Giant electrostriction and relaxor ferroelectric behavior in electron-irradiated poly (vinylidene fluoride-trifluoroethylene) copolymer. Science 280, 2101–2104 5372.

Zhao, X., Suo, Z., 2009. Electromechanical instability in semicrystalline polymers. Appl. Phys. Lett. 95 (3), 031904.

Zhao, X., Wang, Q., 2014. Harnessing large deformation and instabilities of soft dielectrics: Theory, experiment, and application. Appl. Phys. Rev. 1 (2), 021304.